

Spatial scale-aware tail dependence modeling for high-dimensional spatial extremes

Muyang Shi¹, Likun Zhang², Mark D. Risser³, Benjamin A. Shaby¹

Abstract

Extreme events over large spatial domains may exhibit highly heterogeneous tail dependence characteristics, yet most existing spatial extremes models yield only one dependence class over the entire spatial domain. To accurately characterize “data-level dependence” in analysis of extreme events, we propose a mixture model that achieves flexible dependence properties and allows high-dimensional inference for extremes of spatial processes. We modify the popular random scale construction that multiplies a Gaussian random field by a single radial variable; we allow the radial variable to vary smoothly across space and add non-stationarity to the Gaussian process. As the level of extremeness increases, this single model exhibits both asymptotic independence at long ranges and either asymptotic dependence or independence at short ranges. We make joint inference on the dependence model and a marginal model using a copula approach within a Bayesian hierarchical model. Three different simulation scenarios show close to nominal frequentist coverage rates. Lastly, we apply the model to a dataset of extreme summertime precipitation over the central United States. We find that the joint tail of precipitation exhibits non-stationary dependence structure that cannot be captured by limiting extreme value models or current state-of-the-art sub-asymptotic models.

Keywords: Asymptotic dependence, Nonstationary, Scale mixture, Spatial extremes

1 Introduction

Accurately characterizing the spatial extent and intensity of large-scale extreme precipitation events is a critical factor in infrastructure planning, risk mitigation, and adaptation (Field et al., 2014), particularly in our changing global climate (Milly et al., 2008). In this paper, we propose a highly flexible tail dependence model that modulates a radial variable to introduce varying levels of dependence strength both locally and across long spatial ranges, and incorporates a nonstationary covariance function to further account for spatial heterogeneity. Our sub-asymptotic framework

¹Colorado State University

²University of Missouri

³Lawrence Berkeley National Lab

summarizes the tail dependence structure in a parsimonious manner and allows for efficient inference from large spatial data sets. Therefore, we can appropriately model the varying scale and intensity of extreme precipitation events.

Let $\{Y(\mathbf{s}) : \mathbf{s} \in \mathcal{S} \subseteq \mathbb{R}^2\}$ be the stochastic process of interest, and denote its realization at the j th location \mathbf{s}_j by $Y_j = Y(\mathbf{s}_j)$, $j = 1, \dots, D$. In a spatial extremes context, a common approach is to model the marginal distributions of each Y_j (denoted by F_j) separately from their dependence structure via the copula. After transforming the data to the uniform scale via the probability integral transform, a carefully chosen spatial dependence model can be used to accurately characterize the tail dependence properties of the copula while accounting for spatial non-stationarity.

Unfortunately, previous spatial extremes models have dependence structures that are too rigid for large domains and thus lead to underestimation or overestimation of the spatial extent and intensity of extreme events (Huser and Genton, 2016). Statistical modeling for spatial extremes traditionally uses either max-stable processes (when considering block maxima) or generalized Pareto processes (for exceedances of a high threshold) due to their asymptotic justifications (Davison et al., 2013; Huser and Wadsworth, 2022). The copulas of both processes exhibit stability properties, wherein their dependence structures are invariant to the operations of taking maxima over larger blocks or conditioning on a higher threshold. In the bi-variate case, this means that the upper dependence measure of the process between any two locations \mathbf{s}_i and \mathbf{s}_j

$$\chi_{ij}(u) = P(F_j(Y_j) > u \mid F_i(Y_i) > u) \tag{1}$$

will always have a non-zero limit as the quantile level $u \rightarrow 1$, a property generally referred to as asymptotic dependence (AD). Max-stable and generalized Pareto models also have the property that $\chi_{ij}(u)$ becomes independent of u for increasingly extreme events. However, for sub-asymptotic modeling, both of these properties are often violated empirically: estimates of (1) tend to decrease with u for many observed environmental processes, including high-frequency wave height data (Huser and Wadsworth, 2019), daily fire weather indices (Zhang et al., 2021), annual maximum temperature (Zhang et al., 2024), and extreme seasonal precipitation (see Figure 1). Furthermore, weakening $\chi_{ij}(u)$ in the empirical estimates as $u \rightarrow 1$ may eventually result in asymptotic independence (AI), i.e., $\lim_{u \rightarrow 1} \chi_{ij}(u) = 0$. Of course, empirically weakening $\chi_{ij}(u)$ as u approaches its observed upper bound does not necessarily correspond to asymptotic independence since estimates of $\chi_{ij}(u)$ for large u have very large uncertainty and may not suggest convergence in the limit.

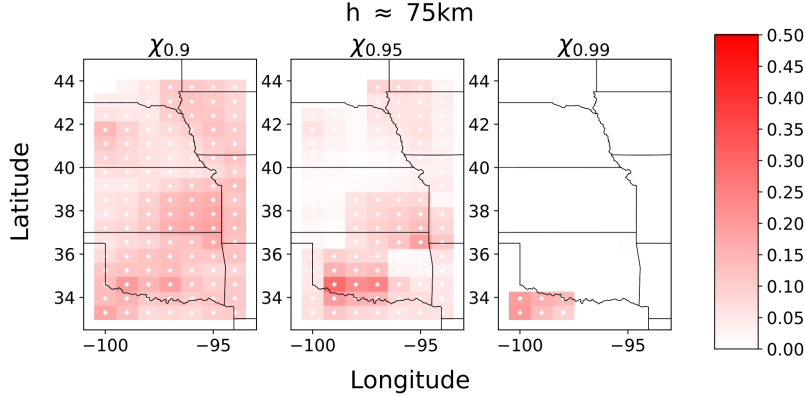


Figure 1: Empirical estimates of $\hat{\chi}_h(u)$ from 75 years of summertime maximum daily precipitation of central US within moving windows centered at 119 locations (marked as white ‘+’), using all pairs with separating distance $\approx 75\text{km}$, at three quantile levels $u = 0.9, 0.95, 0.99$. The local tail dependence behavior appears to vary across the region. Further exploration is shown in Figure 10 in Section 4.

To avoid having to specify the dependence class before analyzing a specific data set, a series of flexible models have been developed to encompass both AI and AD dependence classes (e.g., Huser et al., 2017; Huser and Wadsworth, 2019). The general form of the spatial dependence model in these approaches is

$$X(\mathbf{s}) = R \cdot g(Z(\mathbf{s})), \quad R | \theta_R \sim F_R, \quad (2)$$

in which R is a random scaling factor whose distribution function F_R is parameterized by the vector θ_R containing a parameter ϕ which controls its tail heaviness, $g(\cdot)$ is a suitable link function, and $\{Z(\mathbf{s})\}$ is a stationary spatial process exhibiting asymptotic independence at any two locations. Intuitively, R is a completely dependent spatial process that amplifies the co-occurrences of extreme events in $\{Z(\mathbf{s})\}$, and the tail behavior of $X(\mathbf{s})$ is controlled by the relative rate of tail decay between R and $\{g(Z(\mathbf{s}))\}$ (Engelke et al., 2019). Consequently, random scale mixture models are able to smoothly traverse from asymptotic independence to asymptotic dependence through controlling the tail index ϕ . In spite of this desirable property, inference for random scale mixture models is challenging. To mitigate computational burden while preserving tail dependence properties, Zhang et al. (2021) proposed the addition of a nugget effect which facilitates likelihood calculations for large data sets. Nevertheless, the random scale mixture models in (2) may lack sufficient flexibility because they can only exhibit one dependence class, at all spatial lags, for the entire spatial domain. Coupled with the stationarity of the latent process $\{Z(\mathbf{s})\}$, this means that the dependence measure for any two locations is also stationary (i.e., $\chi_{ij}(u) \equiv \chi_{\|\mathbf{s}_i - \mathbf{s}_j\|}(u)$). Such assumptions of stationarity in both the dependence class of $X(\cdot)$ and the length scales of $Z(\cdot)$ are convenient but are rarely

appropriate for heterogeneous real-world data sets. The assumption that the tail dependence is of the same asymptotic class at all spatial lags seems unintuitive for large domains, where a process may have very strong tail dependence at short distances but weak tail dependence at long distances.

To introduce non-stationarity in the tail dependence structure, [Castro-Camilo and Huser \(2020\)](#) let the dependence parameter ϕ be a spatial process $\phi(\mathbf{s})$ that alters the amplifying effect of R over space. Their specification is in the form of random location mixture, which is equivalent to a random scale mixture through an exponential marginal transformation:

$$X(\mathbf{s}) = \phi^{-1}(\mathbf{s})R + Z(\mathbf{s}), \mathbf{s} \in \mathcal{S}. \quad (3)$$

They furthermore specify $\{Z(\mathbf{s})\}$ to be a zero-mean Gaussian process with a nonstationary Matérn covariance function ([Paciorek and Schervish, 2006](#)), resulting in a non-stationary dependence measure χ_{ij} for locations \mathbf{s}_i and \mathbf{s}_j . While this model yields much more flexible local dependence properties, χ_{ij} is always strictly positive unless $\max\{\phi_i, \phi_j\} = \infty$; i.e., this model still exhibits asymptotic dependence everywhere, even for locations that are very far apart.

To address this limitation, [Hazra et al. \(2024\)](#) generalizes the [Huser et al. \(2017\)](#) model by instead allowing R to be a spatial process and ϕ a spatial constant:

$$X(\mathbf{s}) = R(\mathbf{s})Z(\mathbf{s}), \mathbf{s} \in \mathcal{S}, \quad (4)$$

where $Z(\mathbf{s})$ is a zero-mean isotropic Gaussian process, and $R(\mathbf{s})$ is a kernel-weighted sum of univariate random effects. The kernels live in same spatial domain as the data and are compact, resulting in AI of the $X(\mathbf{s})$ process for locations sufficiently far apart (see our [Theorem 2.3](#) for our analogous result). Their random effects distribution contains a tail parameter $\phi \geq 0$ such that $\phi = 0$ gives AI for locations close enough to share a common kernel. The model in [Hazra et al. \(2024\)](#) represents a major step forward in the flexibility of spatial extremes methods in that it combines local AD with long-range AI. However, we improve upon their approach in several ways. First, we use a different random effects distribution, which allows the transition between local AI and AD to occur in the interior of its parameter space. In contrast, whereas we are able to estimate the local tail dependence class, [Hazra et al. \(2024\)](#) only consider $\phi = 0$ in their analysis, which fixes the dependence class to be AD at short ranges. For highly heterogeneous weather processes like extreme precipitation, it is often far from clear that local asymptotic dependence is always realistic, as seen in [Figure 1](#). Second, our random effects specification also permits a richer set of analytical results than is contained in [Hazra et al. \(2024\)](#), including results on sub-asymptotic tail dependence in the local

AI case. Furthermore, we allow the tail parameter ϕ to vary in space, similarly to [Castro-Camilo and Huser \(2020\)](#). This can be important, as empirical estimates of the dependence class for our precipitation data suggests that it may exhibit both local AI and local AD in different parts of the domain; see again [Figure 1](#).

Finally, the way [Hazra et al. \(2024\)](#) handle marginal fitting is computationally convenient but induces a few modeling disadvantages which we avoid. Specifically, they perform location-specific standardization of the data before model fitting, then assume that the standardized observations follow a location-scale transformation of their dependence model $X(\mathbf{s})$. Such a scheme does not allow for spatial prediction, since the site-specific standardization leaves no way to “de-standardize” any model-predicted $X(\mathbf{s})$ at un-observed locations. More worryingly, assuming the data follow a location-scale transformation of $X(\mathbf{s})$ forces the marginal tail weight of the observations to coincide with the marginal weight behavior of the dependence model $X(\mathbf{s})$. This inextricably couples the marginal and dependence properties, a situation that we would like to avoid. In contrast, we perform full joint inference on the marginal and dependence models using a copula approach. While this requires a good deal more implementation effort, it allows natural spatial prediction and prevents characteristics of the marginal tail weight from bleeding into the fit of the dependence parameters.

[Majumder et al. \(2024\)](#) also use a construction like [\(4\)](#), but $R(\mathbf{s})$ is specified as a max-stable process. This yields short-range AD and long-range AI, but their model presents challenges. First, analytical results are elusive, so tail dependence properties must be confirmed through simulation. More importantly, likelihoods are unavailable, so [Majumder et al. \(2024\)](#) use a Vecchia-type approximation ([Vecchia, 1988](#)) along with neural net emulators to perform approximate Bayesian inference.

[Wadsworth and Tawn \(2022\)](#) use a completely different approach to obtain flexible models capable of short-range AD and long-range AI. They specify their model conditionally on observing a large value at a single reference location. Since there is usually no natural location to choose as the reference, [Wadsworth and Tawn \(2022\)](#) form composite likelihoods by choosing several sites in turn, and summing the log likelihoods obtained from each. This has the effect of fitting a model that requires conditioning on a single site, but uses the composite likelihood to do a kind of averaging across different choices of conditioning sites when fitting model parameters. This approach is an important advancement that generates very flexible tail dependence characteristics.

However, because the resultant fits do not correspond to any well-defined joint probability model, interpretation is challenging.

2 Model

2.1 Construction

Here, we combine the desirable features of (3) and (4) by allowing both $R(\mathbf{s})$ and $\phi(\mathbf{s})$ to vary spatially by using a mixture component representation for $R(\mathbf{s})$ and a spatially-varying tail index $\phi(\mathbf{s})$ in order to introduce more flexible local and long-range tail dependence behaviors:

$$X(\mathbf{s}) = R(\mathbf{s})^{\phi(\mathbf{s})}g(Z(\mathbf{s})), \quad (5)$$

where $\{Z(\mathbf{s})\}$ is a spatial process with hidden regular variation (Ledford and Tawn, 1996; Heffernan and Resnick, 2005). The hidden regular variation assumption ensures

$$P(F_i^Z(Z_i) > u, F_j^Z(Z_j) > u) = L_Z\{(1-u)^{-1}\}(1-u)^{1/\eta_{ij}^Z}, \quad (6)$$

where $\eta_{ij}^Z \in (1/2, 1)$ so that (Z_i, Z_j) exhibits asymptotic independence, F_j^Z is the univariate distribution function of Z_j , $j = 1, \dots, D$, and L_Z is a slowly varying function, i.e., $L_Z(tz) / L_Z(z) \rightarrow 1$ as $z \rightarrow \infty$ for all fixed $t > 0$. The coefficient η_{ij}^Z was termed the *coefficient of tail dependence* for $\{Z(\mathbf{s})\}$ between \mathbf{s}_i and \mathbf{s}_j by Ledford and Tawn (1996), and it complements (1) in the case of asymptotic independence.

In (5), both the scaling factor and the tail index vary across space. This makes the model much more flexible but also adds considerable complexity to both the theoretical analysis and the computations. The theoretical tools used to analyze models where either the scaling factor (Hazra et al., 2024) or the tail index (Castro-Camilo and Huser, 2020), but not both, vary spatially, will not suffice here. However, if the random factors are weighted averages of Stable random variables (Nolan, 2020), the analysis is simplified considerably. Let

$$R(\mathbf{s}) = \sum_{k=1}^K w_k(\mathbf{s}, r_k) S_k, \quad S_k \stackrel{\text{indep}}{\sim} \text{Stable}(\alpha, 1, \gamma_k, \delta), \quad (7)$$

in which $w_k(\mathbf{s}, r_k)$ is some compactly supported basis function over \mathbb{R}^2 centered at the k th knot with radius r_k , $k = 1, \dots, K$. Also, $\sum_{k=1}^K w_k(\mathbf{s}; r_k) = 1$ for all $\mathbf{s} \in \mathcal{S}$. Properties of the univariate and joint distribution of the constructed $\{X(\mathbf{s})\}$ and interpretation of its parameters are discussed in Section 2.2 and 2.3. The link function $g(\cdot)$ transforms the margins of $\{Z(\mathbf{s})\}$ to the margins of a type II Pareto distribution whose distribution function is

$$F^{\text{Pareto}}(x) = \{1 - (1 + x - \delta)^{-1}\} \mathbb{1}(x \geq \delta). \quad (8)$$

We provide justifications for these distributional choices in the subsequent sections.

2.2 Univariate distribution of the dependence model

The key property of the Stable distribution which allows us to assess the tail behavior of the dependence model $X(\mathbf{s})$ in (5) is that it is closed under convolution; if $S_k \stackrel{\text{indep}}{\sim} \text{Stable}(\alpha, \beta_k, \gamma_k, \delta_k)$ and constant $w_k \geq 0$ for $k = 1, \dots, K$, then

$$\sum_{k=1}^K w_k S_k \sim \text{Stable}(\alpha, \bar{\beta}, \bar{\gamma}, \bar{\delta}) \quad (9)$$

with $\bar{\gamma} = \{\sum_{k=1}^K (w_k \gamma_k)^\alpha\}^{1/\alpha}$, $\bar{\beta} = \sum_{k=1}^K \beta_k (w_k \gamma_k)^\alpha / \bar{\gamma}^\alpha$ and $\bar{\delta} = \sum_{k=1}^K w_k \delta_k$. To be able to examine the joint distribution of (X_i, X_j) for model (5), it is desirable for the mixture to have the same distributional support and rate of tail decay as each S_k . Thus in (7), we fixed $\beta_k \equiv 1$, $\delta_k \equiv \delta$ while imposing the constraint $\sum_{k=1}^K w_k = 1$. As a result, $\bar{\beta} = 1$ and $\bar{\delta} = \delta$, which means the univariate support of the $\{R(\mathbf{s})\}$ is $[\delta, \infty)$ everywhere. We also have tail-stationarity for $\{R(\mathbf{s})\}$ because $P(R(\mathbf{s}) > x) \sim 2\bar{\gamma}^\alpha(\mathbf{s})C_\alpha x^{-\alpha}$ for all $\mathbf{s} \in \mathcal{S}$ as $x \rightarrow \infty$, where $\bar{\gamma}(\mathbf{s}) = [\sum_{k=1}^K \{w_k(\mathbf{s}, r_k)\gamma_k\}^\alpha]^{1/\alpha}$.

With the understanding of the distributions of $\{R(\mathbf{s})\}$, the tail behavior of the univariate distributions of the dependence model (5) can be assessed. To avoid clutter, we denote $X_j := X(\mathbf{s}_j)$, $R_j := R(\mathbf{s}_j)$, and $W_j := g(Z(\mathbf{s}_j))$, $j = 1, \dots, D$.

Proposition 2.1. *The univariate distribution of the process (5) at a location \mathbf{s}_j satisfies*

$$1 - F_j(x) = P\{R_j^{\phi_j} g(Z_j) > x\} \sim \begin{cases} E(R_j^{\phi_j})x^{-1}, & \text{if } 0 \leq \phi_j < \alpha, \\ \frac{2C_\alpha \bar{\gamma}_j^\alpha}{1 - \alpha/\phi_j} x^{-\frac{\alpha}{\phi_j}}, & \text{if } \phi_j > \alpha, \\ 2C_\alpha \bar{\gamma}_j^\alpha x^{-1} \log x, & \text{if } \phi_j = \alpha, \end{cases} \quad (10)$$

as $x \rightarrow \infty$, where $C_\alpha = \Gamma(\alpha) \sin(\alpha\pi/2)/\pi$.

2.3 Joint distribution of the dependence model

We start by considering the joint behavior of two scaling variables, R_i and R_j (defined as kernel-weighted linear combinations of iid Stable random variables in (7)) at two locations \mathbf{s}_i and \mathbf{s}_j . For notational simplicity, we denote $w_{kj} = w_k(\mathbf{s}_j, r_k)$, $k = 1, \dots, K$, and write $\mathbf{w}_j = (w_{1j}, \dots, w_{Kj})$ and $\mathcal{C}_j = \{k : w_{ki} \neq 0, k = 1, \dots, K\}$, $j = 1, \dots, D$. Also denote $\bar{\gamma}_j = \bar{\gamma}(\mathbf{s}_j) = \{\sum_{k=1}^K (w_{kj}\gamma_k)^\alpha\}^{1/\alpha}$. We require that any location $\mathbf{s} \in \mathcal{S}$ is covered by at least one basis function, thus \mathcal{C}_j cannot be empty for any j . The following proposition describes the dependence between two scaling variables R_i and R_j :

Proposition 2.2. (a) *If $\mathcal{C}_i \cap \mathcal{C}_j = \emptyset$, R_i and R_j are independent and $P(R_i > x, R_j > x) \sim$*

$$4C_\alpha^2 \{\bar{\gamma}_i^\alpha\} \left\{ \bar{\gamma}_j^\alpha \right\} x^{-2\alpha} \text{ as } x \rightarrow \infty. \text{ If } \mathcal{C}_i \cap \mathcal{C}_j \neq \emptyset, \text{ then}$$

$$P(R_i > x, R_j > x) = 2C_\alpha C_K(\mathbf{w}_i, \mathbf{w}_j, \boldsymbol{\gamma}) x^{-\alpha}, \quad (11)$$

where $C_K(\mathbf{w}_i, \mathbf{w}_j, \boldsymbol{\gamma}) = \sum_{k=1}^K w_{k,\wedge}^\alpha \gamma_k^\alpha$ with $w_{k,\wedge} = \min(w_{ki}, w_{kj})$, $k = 1, \dots, K$.

(b) If $\mathcal{C}_i \cap \mathcal{C}_j \neq \emptyset$, we have for two positive constants $\phi_i < \phi_j$ and any $c_i, c_j > 0$

$$P(\min(c_i R_i^{\phi_i}, c_j R_j^{\phi_j}) > x) \sim d_\wedge x^{-\alpha/\phi_i}, \quad P(\max(c_i R_i^{\phi_i}, c_j R_j^{\phi_j}) > x) \sim d_\vee x^{-\alpha/\phi_j}, \quad (12)$$

where

$$2C_\alpha \sum_{k \in \mathcal{C}_i \cap \mathcal{C}_j} (w_{ki} \gamma_k)^\alpha c_i^{\alpha/\phi_i} \leq d_\wedge \leq 2^{\alpha+1} C_\alpha \sum_{k \in \mathcal{C}_i} (w_{ki} \gamma_k)^\alpha c_i^{\alpha/\phi_i},$$

$$2C_\alpha \sum_{k \in \mathcal{C}_i \cap \mathcal{C}_j} (w_{kj} \gamma_k)^\alpha c_j^{\alpha/\phi_j} \leq d_\vee \leq 2^{\alpha+1} C_\alpha \sum_{k \in \mathcal{C}_j} (w_{kj} \gamma_k)^\alpha c_j^{\alpha/\phi_j}.$$

Remark 1. If \mathbf{s}_i and \mathbf{s}_j are so distant that $\mathcal{C}_i \cap \mathcal{C}_j = \emptyset$, R_i and R_j are completely independent and hence $\chi_{ij}^R = 0$. If there is at least one basis function that covers both \mathbf{s}_i and \mathbf{s}_j , $\chi_{ij}^R = \lim_{x \rightarrow \infty} P(R_j > x | R_i > x) = C_K(\mathbf{w}_i, \mathbf{w}_j, \boldsymbol{\gamma}) / \bar{\gamma}_i^\alpha > 0$, which means R_i and R_j are asymptotically dependent.

In the following theorem, we describe the tail dependence properties of our proposed model given in Section 2. It shows that the model can be simultaneously AD (or AI) at short spatial distances and AI at long spatial distances. It makes precise how the interplay between the compact kernels and the spatially varying tail parameter $\phi(\mathbf{s})$ determine the class and strength of the spatial tail dependence. Using the existing results on regular variation from Breiman (1965), Cline (1986) and Engelke et al. (2019), it presents bounds for the dependence coefficients χ_{ij} and η_{ij} , which depend on the spatial separation of the locations \mathbf{s}_i and \mathbf{s}_j , the configuration of the compact kernels, and the value of the tail parameter $\phi(\mathbf{s})$ at \mathbf{s}_i and \mathbf{s}_j .

Theorem 2.3. Under the definitions and notation established in the previous sections, for locations \mathbf{s}_i and \mathbf{s}_j , we denote

$$v_{ki} = \frac{(w_{ki} \gamma_k)^\alpha}{\sum_{k \in \mathcal{C}_i} (w_{ki} \gamma_k)^\alpha}, \quad v_{kj} = \frac{(w_{kj} \gamma_k)^\alpha}{\sum_{k \in \mathcal{C}_j} (w_{kj} \gamma_k)^\alpha},$$

and $v_{k,\wedge} = \min(v_{ki}, v_{kj})$, $v_{k,\vee} = \max(v_{ki}, v_{kj})$. Also, let $W_j = g(Z_j)$, $j = 1, \dots, D$.

(a) If $\mathcal{C}_i \cap \mathcal{C}_j \neq \emptyset$, the dependence class of the pair $(X_i, X_j)^T$ depends on the tail index parameters ϕ_i and ϕ_j .

(i) If $\alpha < \phi_i < \phi_j$, the pair $(X_i, X_j)^T$ is asymptotically dependent with $\eta_{ij} = 1$ and

$$\chi_{ij} = E \left\{ \min \left(\frac{W_i^{\alpha/\phi_i}}{E(W_i^{\alpha/\phi_i})}, \frac{W_j^{\alpha/\phi_j}}{E(W_j^{\alpha/\phi_j})} \right) \right\} \sum_{k=1}^K v_{k,\wedge}.$$

(ii) If $\phi_i < \phi_j < \alpha$, the pair $(X_i, X_j)^T$ is asymptotically independent with $\chi_{ij} = 0$ and

$$\begin{cases} \eta_{ij} = \eta_{ij}^W, & \text{if } \eta_{ij}^W > \phi_j/\alpha, \\ \eta_{ij} \in [\eta_{ij}^W, \phi_j/\alpha], & \text{if } \phi_i/\alpha < \eta_{ij}^W < \phi_j/\alpha, \\ \eta_{ij} \in [\phi_i/\alpha, \phi_j/\alpha], & \text{if } \eta_{ij}^W < \phi_i/\alpha. \end{cases}$$

(iii) If $\phi_i < \alpha < \phi_j$, the pair $(X_i, X_j)^T$ is also asymptotically independent with $\chi_{ij} = 0$ and

$$\begin{cases} 1/\eta_{ij} \in [(1 - \phi_i/\alpha)/(2\eta_{ij}^W) + 1, 2 - \phi_i/\alpha], & \text{if } \eta_{ij}^W \leq (\phi_i/\alpha + \phi_j/\alpha)/2, \\ 1/\eta_{ij} \in [(1 + \phi_j/\alpha)/(2\eta_{ij}^W), 2 - \phi_i/\alpha], & \text{if } \eta_{ij}^W > (\phi_i/\alpha + \phi_j/\alpha)/2. \end{cases}$$

(b) If $\mathcal{C}_i \cap \mathcal{C}_j = \emptyset$, the pair $(X_i, X_j)^T$ is asymptotically independent with $\chi_{ij} = 0$. When $\rho_{ij} = 0$, X_i and X_j are completely independent. When $\rho_{ij} \neq 0$,

(i) If $\alpha < \phi_i < \phi_j$,

$$\begin{cases} \eta_{ij} = 1/2, & \text{if } \phi_i/\alpha > 2, \\ \eta_{ij} \in [1/2, \alpha/\phi_i], & \text{if } \phi_i/\alpha < 2 < \phi_j/(\alpha\eta_{ij}^W), \\ \eta_{ij} \in [\alpha\eta_{ij}^W/\phi_j, \alpha/\phi_i], & \text{if } \phi_j/(\alpha\eta_{ij}^W) < 2. \end{cases}$$

(ii) If $\phi_i < \phi_j < \alpha$, the pair $(X_i, X_j)^T$ is asymptotically independent with $\chi_{ij} = 0$ and

$$\begin{cases} \eta_{ij} = \eta_{ij}^W, & \text{if } \eta_{ij}^W > \phi_j/\alpha, \\ \eta_{ij} \in [\eta_{ij}^W, \phi_j/\alpha], & \text{if } \eta_{ij}^W < \phi_j/\alpha. \end{cases}$$

(iii) If $\phi_i < \alpha < \phi_j$, the pair $(X_i, X_j)^T$ is also asymptotically independent with $\chi_{ij} = 0$ and

$$\begin{cases} 1/\eta_{ij} \in [1/(1 + \rho_{ij}) + 1, 2], & \text{if } 2\eta_{ij}^W \leq \phi_j/\alpha, \\ 1/\eta_{ij} \in [(1 + \phi_j/\alpha)/(1 + \rho_{ij}), 2], & \text{if } 2\eta_{ij}^W > \phi_j/\alpha. \end{cases}$$

Remark 2. In Theorem 2.3(a), when $\mathcal{C}_i \cap \mathcal{C}_j \neq \emptyset$, both AD and AI are possible as the dependence strength is controlled by both $(\phi_i, \phi_j)^T$ and the weights $(\mathbf{w}_i^T, \mathbf{w}_j^T)^T$. Roughly speaking, larger $\min\{\phi_i, \phi_j\}$ or smaller $\|\mathbf{w}_i - \mathbf{w}_j\|$ induces stronger dependence. Additionally, when $\mathcal{C}_i \cap \mathcal{C}_j = \emptyset$, the dependence structure of $(Z_i, Z_j)^T$ is recovered.

Remark 3. Theorem 2.3 suggests a natural interpretation of the spatially varying tail parameter $\phi(\mathbf{s})$. For a given location \mathbf{s}_i , if $\phi(\mathbf{s}_i)$ is larger than α , then $X(\mathbf{s}_i)$ is asymptotically dependent with $X(\mathbf{s}_j)$ at location \mathbf{s}_j , provided that $\phi(\mathbf{s}_i)$ is also larger than α and \mathbf{s}_i shares a kernel with \mathbf{s}_j . However, if $\phi(\mathbf{s}_i)$ is smaller than α , then $X(\mathbf{s}_i)$ can never be asymptotically dependent with any other location. Therefore, the surface $\phi(\mathbf{s})$ represents the *potential strength of tail dependence* of the process at all locations \mathbf{s} with any other location.

2.4 Examples

In this section, we provide a few concrete examples for the dependence model $\{X(\mathbf{s})\}$ defined in (5) and selections for the Stable variable parameters.

Example 1 (Huser and Wadsworth (2019) process). This is a scale mixture model defined in (2) where $\{Z(\mathbf{s})\}$ is a stationary spatial process with hidden regular variation, the link function $g(\cdot)$ transforms the margins of $\{Z(\mathbf{s})\}$ to standard Pareto (corresponding to $\delta = 1$ in (8)) and

$$R | \phi^H \sim \text{Pareto} \left(\frac{1 - \phi^H}{\phi^H} \right), \quad \phi^H \in [0, 1].$$

This model is tail equivalent to a special case of (5) obtained by fixing $K \equiv 1$, $r = \infty$ and $\phi(\mathbf{s}) \equiv \phi$, and also making $\delta = 1$, which means $R(\mathbf{s}) \equiv S_1 \sim \text{Stable}(\alpha, 1, \gamma_1, 1)$. If we denote $\alpha/\phi = (1 - \phi^H)/\phi^H$, the tail behavior in (10) corresponds to that of Equation (9) in Huser and Wadsworth (2019): the case when $\phi \in (0, \alpha)$ corresponds to $\phi^H \in [0, 1/2)$ which induces asymptotic independence, while $\phi \in (\alpha, \infty)$ corresponds to $\phi^H \in (1/2, 1)$ which induces asymptotic dependence. When $\phi = \alpha$, the tail decays with the same order as a Gamma random variable with rate 1 and shape 2, which is the same as the survival function of the case $\phi^H = 1/2$.

Furthermore, since $K \equiv 1$ and $r = \infty$, the interval for η_{ij} from Theorem 2.3(a) reduces to a singleton and we have

$$\chi_{ij} = E \left[\min \left\{ \frac{W_i^{\alpha/\phi}}{E(W_i^{\alpha/\phi})}, \frac{W_j^{\alpha/\phi}}{E(W_j^{\alpha/\phi})} \right\} \right] \mathbb{1}(\phi < \alpha),$$

which is exactly equation (10) in Huser and Wadsworth (2019) given $\alpha/\phi = (1 - \phi^H)/\phi^H$. Similarly, we can show that η_{ij} under the stationary version of (5) is also equivalent to that of Huser and Wadsworth (2019, see their equation (11)).

Example 2 (Huser and Wadsworth (2019) process with spatially-varying R). Similar to the generalization from the Huser et al. (2017) process to model (4) by Hazra et al. (2024), we can allow $K > 1$ and $r < \infty$ while holding the parameters for the Stable variables constant at all knots. That is,

$$\phi(\mathbf{s}) \equiv \phi, S_k \stackrel{\text{iid}}{\sim} \text{Stable}(\alpha, 1, \gamma, \delta), k = 1, \dots, K.$$

To achieve local asymptotic dependence (i.e., scenario Theorem 2.3(a)(i)) with a constant ϕ , the value of ϕ has to be greater than α . Then, as in Hazra et al. (2024), local asymptotic independence is not possible under this construction because $\phi(\mathbf{s}) \equiv \phi > \alpha$ and (a)(i) always holds locally. However, this case achieves more flexible local dependence properties than the model specified in (4) as the value of $\phi \in (\alpha, \infty)$ is not fixed (recall that ϕ has to be fixed at 0 in Hazra et al. (2024) because the Huser et al. (2017) can only achieve asymptotic dependence when $\phi = 0$).

Illustration 1 (Empirical evaluations of the bounds in Theorem 2.3). We simulate $N = 300,000,000$ data sets on the domain $\mathcal{S} = [0, 10] \times [0, 10]$ using a $\{\phi(\mathbf{s}) : \mathbf{s} \in \mathcal{S}\}$ surface that varies smoothly between 0.4 to 0.7; see Figure 2. For each simulation, we generate independent Stable variables with $\alpha = 0.5$ at 9 knots on a uniform grid and average them using compact Wendland basis functions centered at the knots (Wendland, 1995). We empirically estimate the $\chi_{ij}(u)$ and $\eta_{ij}(u)$

functions defined in (1) and (6) between pairs of the sample points on a grid of u values, using the N independent simulations of $(R_i^{\phi_i} W_i, R_j^{\phi_j} W_j)$.

Corresponding to Theorem 2.3(a)(i), Figure 3(a) shows the empirical estimated $\chi_{12}(u)$ and $\eta_{12}(u)$ for the 1st and 2nd sample points over a grid of u . These two points share a common Wendland kernel and $\alpha = 0.5 < \phi_6 < \phi_9$, so they are asymptotically dependent. Corresponding to Theorem 2.3(a)(ii), Figure 3(b) shows the empirical estimated $\chi_{34}(u)$ and $\eta_{34}(u)$ for the 3rd and 4th sample points. These two points share a common Wendland kernel, but $\phi_1 < \phi_2 < \alpha$, so they are asymptotically independent. Figure 3(c) shows the empirical estimated $\chi_{45}(u)$ and $\eta_{45}(u)$ for the 4th and 5th sample points. This corresponds to Theorem 2.3(a)(iii), as the two points also share a common Wendland kernel, yet $\phi_2 < \alpha < \phi_3$, so they are still asymptotically independent. Finally, Figure 3(d) shows the empirical estimated $\chi_{15}(u)$ and $\eta_{15}(u)$ for the 1st and 5th sample points. Corresponding to Theorem 2.3(b)(i), these two locations do not share any common Wendland kernel, so even-though $\phi_9 > \phi_6 > \alpha$, we still have asymptotically independence.

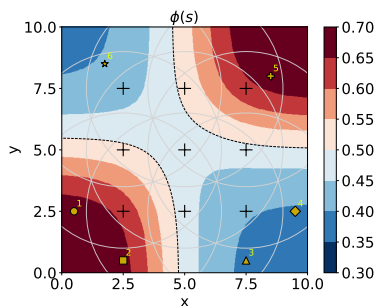


Figure 2: A $\phi(\mathbf{s})$ surface on $[0, 10]^2$, in which the dashed line marks the transition between local AI and AD. The points with ‘+’ are centers for the Stable variables and the compact Wendland basis functions. The points with other signs/marker-styles are randomly chosen sample points that we use to verify the dependence properties in Theorem 2.3.

3 Bayesian inference

We define a Bayesian hierarchical model based on the dependence model (5) in Section 2.1 and use a MCMC algorithm to fit to the data. The dependence model (5) is displayed again here for convenience, now with each time replicate denoted with a subscript $t = 1, \dots, T$:

$$X_t(\mathbf{s}) = R_t(\mathbf{s})^{\phi(\mathbf{s})} g(Z_t(\mathbf{s})).$$

3.1 Hierarchical model

Let $\{Y_t(\mathbf{s}) : \mathbf{s} \in \mathcal{S}, t = 1, \dots, T\}$ denote the spatial process on the scale of the observations. We link this process to our dependence model using a marginal probability integral transform within the hierarchical model as

$$F_{Y|\boldsymbol{\theta}_Y(\mathbf{s}),t}(Y_t(\mathbf{s})) = F_{X|\phi(\mathbf{s}),\bar{\gamma}(\mathbf{s}),t}(X_t(\mathbf{s})). \quad (13)$$

In principle, the dependence model can be used for any marginal distribution. Here we opt for

Schervish, 2006; Risser and Calder, 2015)

$$C(\mathbf{s}, \mathbf{s}') = \zeta(\mathbf{s})\zeta(\mathbf{s}') \frac{\sqrt{\rho(\mathbf{s})\rho(\mathbf{s}')}}{\{\rho(\mathbf{s}) + \rho(\mathbf{s}')\}/2} \mathcal{M}_\nu \left(\frac{\|\mathbf{s} - \mathbf{s}'\|}{\sqrt{\{\rho(\mathbf{s}) + \rho(\mathbf{s}')\}/2}} \right), \quad (15)$$

where the standard deviation process $\zeta(\mathbf{s}) \equiv 1$ for $\mathbf{s} \in \mathcal{S}$, $\mathcal{M}_\nu(\cdot)$ is the Matérn correlation function with range 1 and smoothness ν , and $\rho(\mathbf{s})$ is the spatially varying range parameter.

As described in Section 2.1, we form a spatially varying surface $R(\mathbf{s})$ by combining K compactly supported Wendland kernel functions, each centered at a knot, each scaled by a corresponding Stable variable. In addition, we construct the $\{\phi(\mathbf{s})\}$ and $\{\rho(\mathbf{s})\}$ surfaces using Gaussian kernel functions centered at the knots. The Wendland kernel function is parameterized as $w_k^{(S)}(\mathbf{s}) \propto \left(1 - \frac{\|\mathbf{s} - \mathbf{b}_k^{(S)}\|^2}{r}\right)_+^l$, in which $l = 2$, $\mathbf{b}_k^{(S)}$ are a grid of knots over the spatial domain \mathcal{S} , and r is the radius of the kernel function.

The priors for the dependence model parameters are $\phi_k \stackrel{\text{iid}}{\sim} \text{Beta}(5, 5)$ and $\rho_k \stackrel{\text{iid}}{\sim} \text{halfNormal}(0, 2)$, $k = 1, \dots, K$, where “halfNormal” refers to the positively truncated normal distribution. The Beta prior for ϕ_k is centered at the transition boundary between AI and AD, and places less mass near the edges of the support which correspond to extremely strong or weak dependence scenarios. In the following, we fix the scale parameter γ of the Stable distribution (somewhat arbitrarily) at 0.5. Varying γ does not play any role in modulating the tail dependence characteristics of the model (see Theorem 2.3), so fixing it at a convenient value results in almost no loss of flexibility.

3.2 Simulation and Coverage Analysis

We present simulation results and conduct coverage analysis to investigate whether the MCMC procedure is able to draw accurate inference on model parameters, assuming marginally GEV responses. We use $D = 500$ sites uniformly drawn from the square $\mathcal{S} = [0, 10]^2$ and $\mathcal{T} = 64$ time replicates. The latent Gaussian process $Z_t(\mathbf{s})$ is generated with a locally isotropic, non-stationary Matérn covariance function as specified in Section 3.1, with $\nu = 0.5$. For each time replicate, we specified $K = 9$ knot locations $\{\mathbf{b}_k^{(S)}, k = 1, \dots, K\}$ over a uniform grid in the spatial domain \mathcal{S} . As specified in Section 3.1, we generate independent Lévy random variables with $\gamma_k = 0.5$ at those nine pre-specified knot locations and interpolate them to site locations using the Wendland kernel functions with radius $r = 4$ centered at those knots; see Figure 4 for illustration.

We consider three scenarios for the scaling parameter $\phi(\mathbf{s})$ and the range parameter $\rho(\mathbf{s})$ so that all cases in Theorem 2.3 are represented; we generate the nine ϕ_k and ρ_k at the same nine

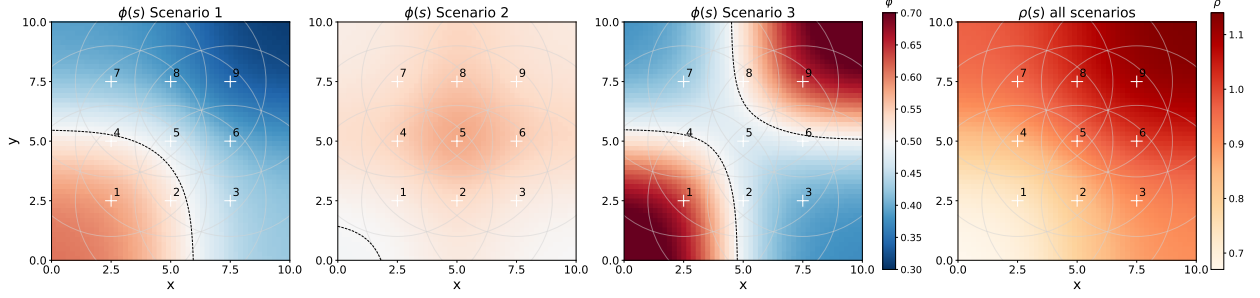


Figure 4: Dependence model parameter surfaces, $\phi(\mathbf{s})$ and $\rho(\mathbf{s})$, for the three simulation scenarios, which correspond to different levels of non-stationarity. The ‘+’ denotes the center of the kernel functions, and the gray circles denotes the radii.

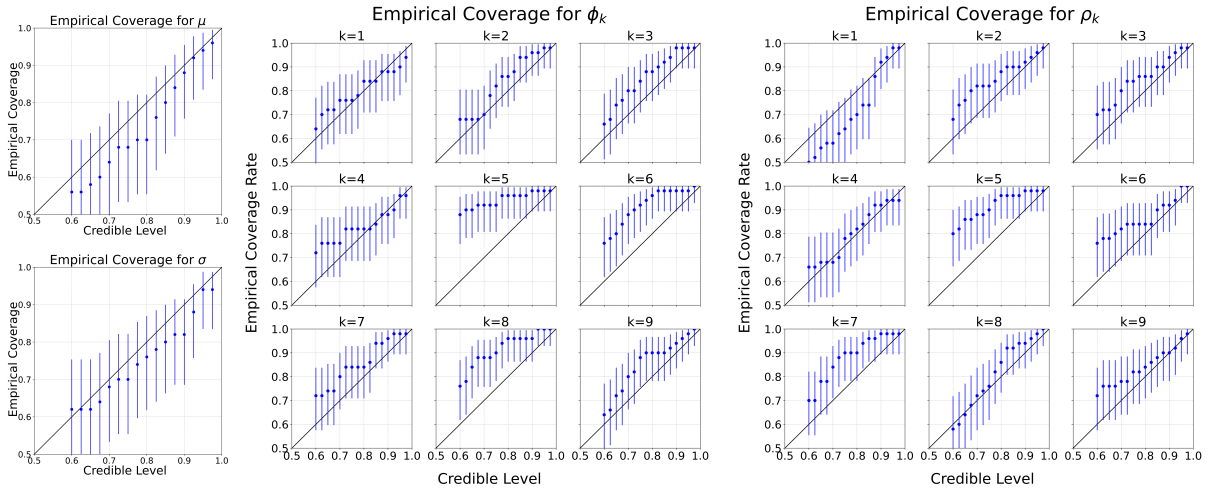


Figure 5: Empirical coverage rates of credible intervals of the marginal parameters μ and σ (left), the dependence parameters ϕ_k (middle), and ρ_k (right), $k = 1, \dots, 9$, in simulation scenario 1.

knots locations ($\mathbf{b}_k^{(S)} = \mathbf{b}_k^{(\phi)} = \mathbf{b}_k^{(\rho)}$), and interpolate them to the site locations using the Gaussian kernel functions with bandwidth $h^{(\phi)} = h^{(\rho)} = 4$ centered at those knots. The interpolated $\{\phi(\mathbf{s})\}$ and $\{\rho(\mathbf{s})\}$ surfaces are shown in Figure 4. Finally, we generated dependence model variables $X_t(\mathbf{s})$ under three scenarios and transformed to marginal GEV distribution with parameters $(\mu(\mathbf{s}), \sigma(\mathbf{s}), \xi(\mathbf{s}))^T = (0, 1, 0.2)^T$. For the purpose of simulations, GEV parameters are set to be spatially and temporally constants with no covariate. For computational expediency in the coverage analysis, $\xi(\mathbf{s})$ is not updated in the simulations.

We study the coverage properties of the posterior inference based on the MCMC samples for the posterior credible intervals with 50 simulated datasets drawn under each of the scenarios. Figure 5 shows the empirical coverage rates of the scaling parameter ϕ and the range parameter ρ at the nine knot locations (i.e. $k = 1, \dots, 9$), as well as the location μ and scale σ of the marginal GEV

parameters in simulation scenario 1. Standard binomial confidence intervals are included on the coverage plots. In all scenarios, we see that the sampler generates well-calibrated posterior inference for the GEV parameters with close to nominal frequentist coverage, and slightly over-covers for the the scaling and range parameters. The Appendix D includes the additional empirical coverage rates of the parameters from simulation scenario 2 and 3 in Figures 11 and 12, which show similar characteristics as the coverage plots from simulation scenario 1.

4 Extreme *in situ* Measurements of Daily Precipitation

4.1 Data Analysis

In this section, we analyze extreme daily measurements from a gauged network of *in situ* weather stations from the Global Historical Climate Network (GHCN; Menne et al., 2012b,a). A subset of the extreme summertime measurements from GHCN stations (see Figure 6(a)) over the central United States was originally analyzed in Zhang et al. (2022) using the Huser and Wadsworth (2019) copula with a spatio-temporally varying marginal model similar to the one we use below. However, exploratory analysis shown in the left-hand panel of Figure 10 suggests that applying a single dependence class to such a large spatial domain is inappropriate, as there are areas in the central U.S. domain where the extreme summer precipitation appear to be locally AI and others that appear to be AD. Furthermore, when applying a single dependence class to the entire domain, Zhang et al. (2022) found that (overall) the extreme precipitation measurements are asymptotically *independent*, meaning that the risk of concurrent extremes would be underestimated for sub-regions that exhibit asymptotic dependence.

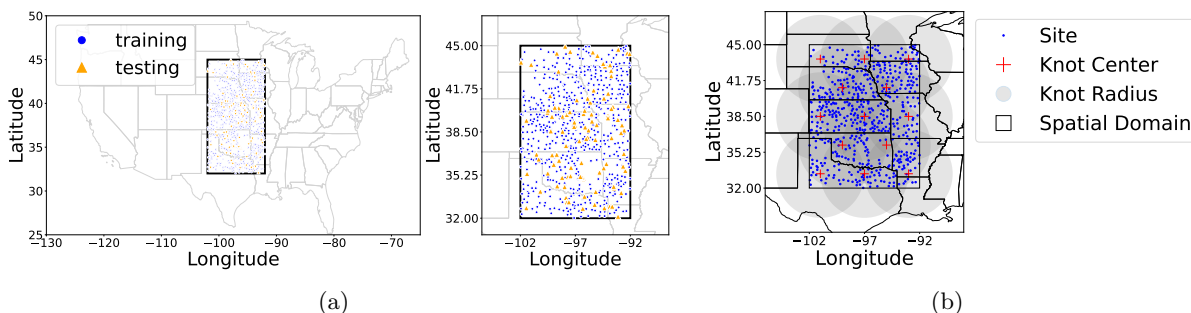


Figure 6: (a) Location of the 590 observations/data sites and the 99 out-of-sample testing sites. (b) An illustration of the mixture component setup for model $k13r4b4$. The blue dots represent observation sites, red '+' symbols represent the centers of the kernel functions, and the shaded circles represent areas covered by each Wendland kernel with specified radius r .

While the GHCN database contains over twenty thousand stations over the contiguous United States, following [Risser et al. \(2019\)](#) we analyze a quality-controlled subset of the network from a recent 75-year period, namely those stations that have a minimum of 90% non-missing daily precipitation measurements over 1949 through 2023. We then restrict our attention to summertime daily measurements (those from June, July, and August, or JJA) in the central United States region (defined by the $[102^\circ\text{W}, 92^\circ\text{W}] \times [32^\circ\text{N}, 45^\circ\text{N}]$ longitude-latitude bounding box), resulting in a set of $D = 590$ stations. Our focus on the central United States in the summer season is intentional, since the majority of extreme precipitation in this region and season results from severe convective storms, which can be highly localized and therefore are particularly challenging to model statistically. Let $P_{tm}(\mathbf{s}_j)$ represent the daily precipitation measurement in millimeters for day $m = 1, \dots, 92$ (the JJA season has 92 days) in year $t = 1949, \dots, 2023$ at station \mathbf{s}_j . We then analyze the summertime maxima, denoted $Y_t(\mathbf{s}_j) = \max_m \{P_{tm}(\mathbf{s}_j)\}$. We only record the JJA maxima at station \mathbf{s}_j in year t if that season has at least 62 non-missing measurements (i.e., at least 66.7% non-missing measurements in JJA) otherwise, $Y_t(\mathbf{s}_j)$ is considered missing.

Corresponding to the block-maxima structured data, we assume that marginally

$$Y_t(\mathbf{s}) \sim \text{GEV}(\mu_t(\mathbf{s}), \sigma_t(\mathbf{s}), \xi_t(\mathbf{s})).$$

To ensure the independence over time and account for potential systematic increase or decrease in rainfall due to global warming, we have assumed a time-varying component for the location parameter. To account for the physical features of the terrain, we incorporate spatially-varying covariate with thin plate splines to smooth over the spatial domain. That is,

$$\mu_t(\mathbf{s}) = \mu_0(\mathbf{s}) + \mu_1(\mathbf{s}) \cdot t, \quad \sigma_t(\mathbf{s}) \equiv \sigma(\mathbf{s}), \quad \xi_t(\mathbf{s}) \equiv \xi(\mathbf{s}),$$

where the spatially varying intercept and slope parameters for the GEV location is specified as a spline as

$$\mu_i(\mathbf{s}) = \beta_0 + \beta_1 \cdot \text{elev}(\mathbf{s}) + \sum_{i=1}^{11} w_i f_{tps}(\mathbf{s}), \quad i \in \{0, 1\},$$

where f_{tps} denotes the thin-plate spline kernel (using 11 degrees of freedom to smooth over the spatial domain). The GEV scale and shape parameters are specified as linear functions of elevation, as

$$\log(\sigma(\mathbf{s})) = \beta_0 + \beta_1 \cdot \text{elev}(\mathbf{s})$$

$$\xi(\mathbf{s}) = \beta_0 + \beta_1 \cdot \text{elev}(\mathbf{s}).$$

We place knots in an isomorphic grid across the spatial domain. We considered eleven different model configurations, consisting of various combinations of different knot grids, different Wendland kernel radii, different Gaussian kernel bandwidths, and restricting the marginal parameters to be spatially constant. Table 1 in Appendix E describes the eleven different setups, and Figure 6(b) illustrates the mixture component setup of the model that we eventually chose.

To obtain MCMC starting values for the marginal parameters, we fit simple GEV regressions, assuming conditional independence across space and time. For the dependence model parameters, we fit empirical variograms to obtain initial values for the range parameter ρ , set $\phi(\mathbf{s})$ to start at 0.5 everywhere, and used the median observation to calculate a starting point for the random scale factor R . We then ran the MCMC chains for approximately 15,000 iterations (or until convergence) such that after discarded a burn-in period, we obtain at least 5,000 posterior samples.

4.2 Model Evaluation

To evaluate model fit, we incorporate additional observations as out-of-sample test data. These stations have $> 85\%$ and $\leq 90\%$ non-missing daily precipitation data measurements over the same time period and spatial domain. The JJA maxima are chosen according to the same criteria as the training dataset, enforcing at least $2/3$ non-missing values in any given year. This results in 99 stations in the test set, drawn as the yellow triangles in Figure 6(a). We evaluate model fit and compare the eleven models based on their predictive log-likelihoods at these 99 stations.

To obtain the log-likelihoods at the out-of-sample sites, draw from predictive distributions of all model parameters at each MCMC iteration. For models that have fixed marginal parameters, we use the initial estimates from the GEV fit to interpolate to the testing sites. Figure 13 in Appendix E displays the boxplots of log-likelihoods at the testing sites for the eleven models we considered. It appears that models which jointly estimate the marginal parameters within the MCMC tend to perform systematically better than models with fixed marginal parameters. This suggests that the common practice of performing the analysis in two steps—first estimating the marginal parameters, then performing the dependence analysis “downstream” by plugging in the empirical marginal estimates to transform the data to convenient margins—is prone to underperform. We believe that it is worth the extra effort to incorporate estimation of the marginal model parameters together with estimation of the dependence model.

We decided to use the *k13r4b4* model based on its superior log-likelihood performance (Figure

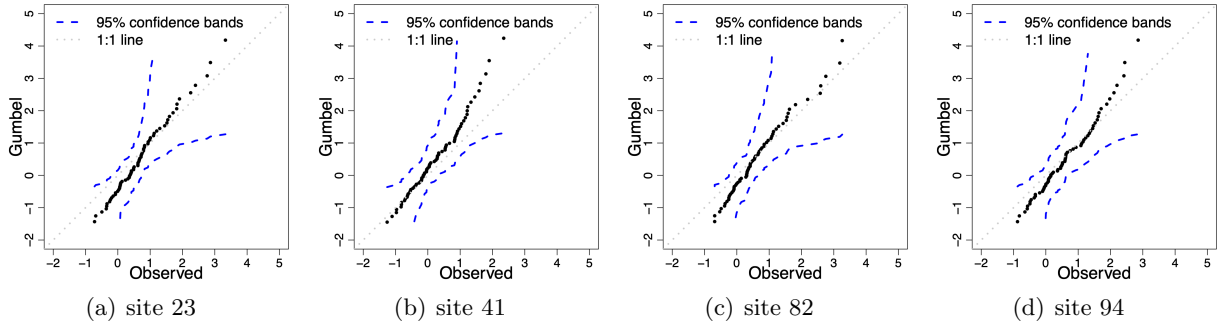


Figure 7: QQ-plots of four members randomly selected from the 99 holdout locations, comparing the observed and predicted marginal quantiles, for the $k13r4b4$ model. Overall 95% confidence envelopes are also shown. Note that the values are transformed marginally to a Gumbel distribution. [13](#) in Appendix E) and its parsimony. The $k25r2b0.67$ model shows comparable performance to our chosen model, but results in overly complex parameter surfaces. We therefore favor the simpler $k13r4b4$ model. In addition, the *stationary* [Huser and Wadsworth \(2019\)](#)-equivalent model performs roughly comparably on average, but with much greater variation. This makes sense based on the posterior mean $\phi(\mathbf{s})$ surface (Figure 8), which varies in space but remains in the AI regime. The [Huser and Wadsworth \(2019\)](#)-equivalent model can capture the overall behavior of the tail dependence strength but not its heterogeneity. Thus, $k13r4b4$ is the most parsimonious candidate model that can still faithfully capture local variation in tail dependence.

In addition, we looked at the empirical quantile plots of the out-of-sample observations to evaluate the model’s marginal fit. Specifically, we compared GEV quantiles based on posterior predictive draws of the marginal parameters at the holdout sites to the empirical quantiles at the same holdout sites. Figure 7 shows QQ-plots from four sites randomly selected from the 99 testing sites, for the best-performing $k13r4b4$ model. The model provides a decent, though not perfect, marginal fit, as the 95% confidence band contains the 1:1 line in each case. Some locations show better marginal fit than others, which is not a surprise since the joint likelihood must balance the joint and marginal fits, rather than exclusively optimizing the marginal fit at each location.

4.3 Results

We now present results from the chosen $k13r4b4$ model. Table 2 in Appendix E reports the posterior means and the 95% equi-tail credible intervals for the dependence parameter $\phi(\mathbf{s})$ and range parameter $\rho(\mathbf{s})$ at the kernel knot locations.

First, we examine the estimates for $\phi(\mathbf{s})$ at the knot locations, specifically whether they fall

within $(0, 1/2]$ or $(1/2, 1)$, corresponding to whether the data-generating process is asymptotically independent or dependent. It appears that this dataset demonstrates asymptotically independent behavior at all spatial ranges with high probability. Recall that the [Hazra et al. \(2024\)](#) cannot capture this behavior. Nonetheless, this is a somewhat disappointing result, as it does not properly highlight one of the key features of our model, which is that it simultaneously allows asymptotic dependence at short distances and asymptotic independence at long distances. However, as the credible intervals for $\phi(\mathbf{s})$ show, there is non-negligible posterior probability that this is the case. The tail dependence also appears to be non-stationary, as the estimated value of $\phi(\mathbf{s})$ changes appreciably over the spatial domain; see [Figure 8](#). Next, the posterior mean $\rho(\mathbf{s})$ surface shows that the correlation range of the latent Gaussian process is estimated to be much longer in some parts of the spatial domain than others. Specifically, southeast Minnesota/northeast Iowa and the Oklahoma panhandle show very short ranges. Finally we include the posterior mean marginal parameter surfaces in [Figure 9](#). Interestingly, the slope parameter $\mu_1(\mathbf{s})$ is positive in about half of the spatial domain and negative in the other half. The largest values correspond to a change of 4.8 millimeters per century in the marginal GEV location. The estimated GEV shape parameter surface shows very little spatial variation and is heavier-tailed than we would have expected.

To assess the tail dependence of the fitted process, we use a moving-window approach, in which we divide the spatial domain into 17×7 sub-regions and empirically estimate and visualize χ in each local window. The left-hand panel of [Figure 10](#) shows the empirical $\hat{\chi}_u(h)$, while the right-hand panel of [Figure 10](#) shows the analogous model-based $\hat{\chi}_u(h)$. To obtain the empirical version, we first use the *k13r4b4* model-fitted marginal GEV parameters to transform the observations $Y_t(s)$ to the $X_t(s)$ scale, then empirically estimate $\hat{\chi}_u(h)$. We do this across three quantile levels, $u = 0.9, 0.95$ and 0.99 , and three distances, approximately 75km, 150km, and 225km. We obtained the analogous model-based version of $\hat{\chi}_u(h)$ by making many unconditional draws from the fitted model, then using the same empirical estimation strategy as in the left-hand panel.

The empirical and model-based estimates of $\chi_u(h)$ show similar spatial patterns, but at different levels. The most prominent feature is the patch of high values along the border between Texas and Oklahoma, as well as the more subtle patch of high values near the border between Nebraska, Iowa, and South Dakota. These features appear in both the left- and right-hand panels of [Figure 10](#). We also notice that as the quantile increases, the estimates $\chi_u(h)$ decrease for all spatial distances,

which is the expected behavior for asymptotic independence. This is consistent with the results shown in Figure 8, which shows that $\phi(\mathbf{s}) < 0.5$ across the entire domain. That the overall level of the model-based $\hat{\chi}_u(h)$ surfaces is higher than that of their empirical analogues, even as the spatial patterns and trends in u are similar, is not terribly concerning; empirical estimates of $\hat{\chi}_u(h)$ are necessarily very noisy, so we would not expect perfect alignment, even if the model perfectly captured the data-generating process.

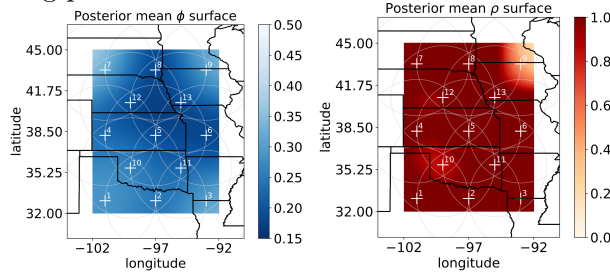


Figure 8: Interpolated surfaces of posterior mean for dependence model: tail dependence parameter $\phi(\mathbf{s})$ and range parameter $\rho(\mathbf{s})$.

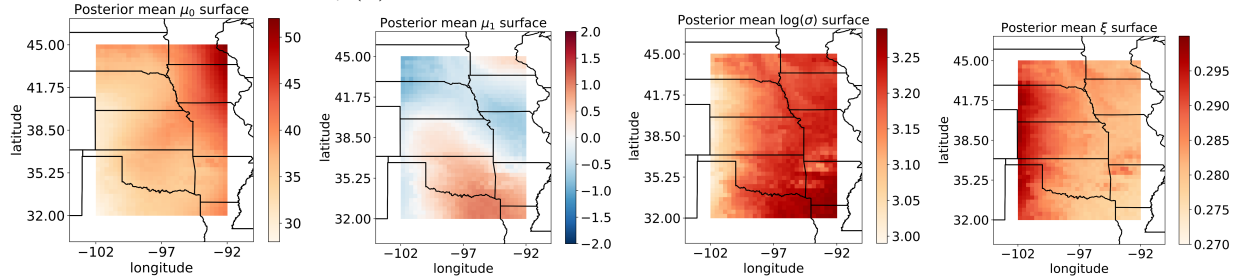


Figure 9: Interpolated surfaces of posterior mean for marginal model parameters.

5 Discussion

In this article, we have proposed a modeling approach that extends the random scale construction to obtain more flexible local and long-range tail dependence behaviors. Our proposed mixture model is capable of simultaneously exhibiting asymptotic independence at long ranges and either asymptotic dependence or independence at short ranges. The model is also able to capture non-stationary tail dependence structure with a spatially varying tail parameter that allows short-range asymptotic independence in some parts of the domain and short-range asymptotic dependence in other parts of the domain. Our model permits trivial unconditional simulation, which easily allows for direct Monte Carlo risk estimates based on complicated functionals like areal sums or extrema. It is also straightforward to do spatial prediction (i.e. interpolation) by drawing from relevant posterior predictive distributions. And because our approach is fully Bayesian, all variation in any

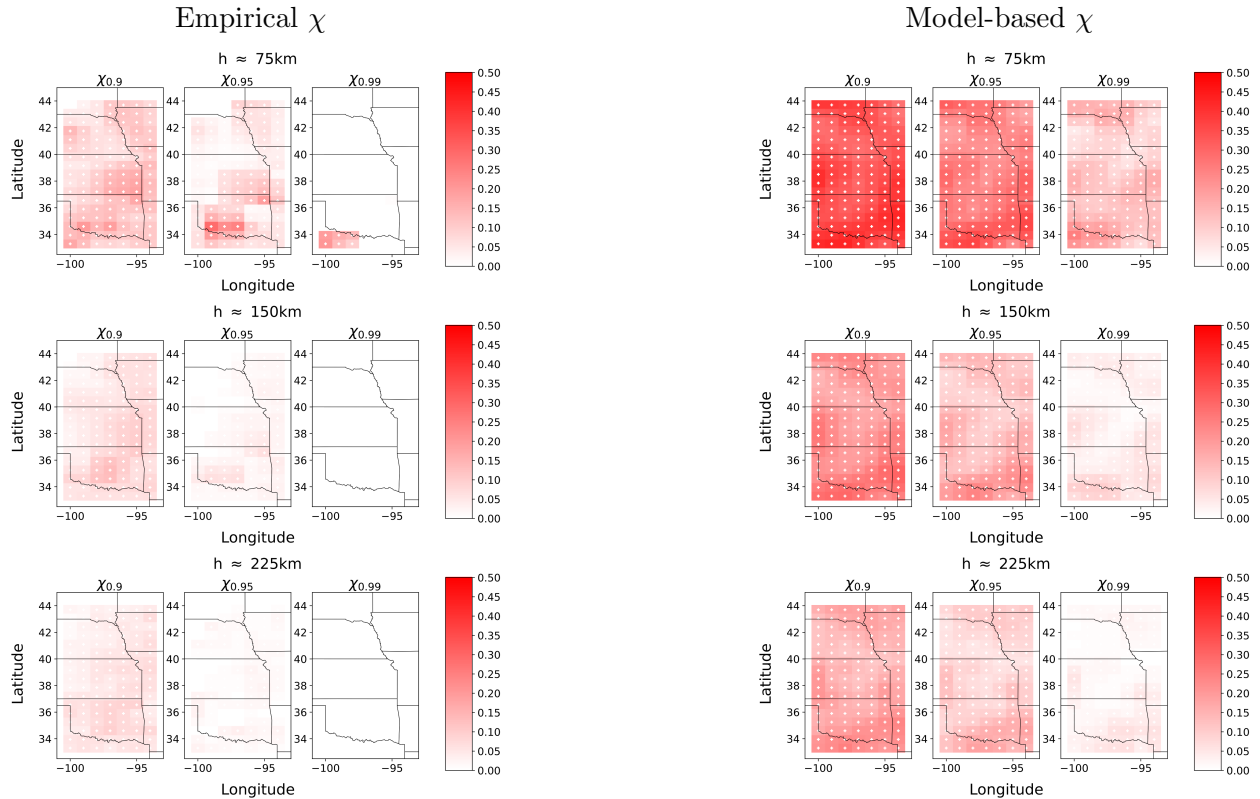


Figure 10: Moving-window estimates of $\chi_u(h)$ across three quantiles u and three spatial lags h . The left-hand panel shows the empirical estimates of $\chi_u(h)$, and the right-hand panel shows the model-based estimates of $\chi_u(h)$, based on the best-performing model *k13r4b4*.

downstream analysis is accounted for in a coherent way.

Our analysis of extreme summertime precipitation in the central US highlighted some of the model’s key features. We expected the data to exhibit short-range asymptotic dependence and long-range asymptotic independence. There was appreciable posterior probability that this was the case, but, somewhat disappointingly, the posterior mean surface of the dependence parameter showed asymptotic independence at all ranges, across the entire spatial domain. Nevertheless, a desirable feature is that any risk estimates based on posterior samples from our model will reflect the ambiguity in the local tail dependence regime.

An interesting side result that merits further study was that models which jointly estimated marginal and dependence parameters always performed better (in holdout set predictive log-likelihoods) than analogous “two-step” models in which marginal parameters were estimated and plugged in before fitting the dependence model. Jointly estimating the marginal and dependence models as we have done incurs large costs in terms of software implementation and computational complexity. However, it seems to confer significant advantages in terms of model fit, in addition to

naturally propagating variation between marginal and dependence models, and on to predictions.

Fitting our model with MCMC allows inference on spatial extreme-value datasets with relatively large numbers of locations. We have defined the model conditionally as a Bayesian hierarchical model, for which standard MCMC techniques can be used. Computation is facilitated by paralleling over time and migrating any required numerical integration to C++. Even so, the lack of closed form marginal transformations creates a significant computational challenge that scales with the total number of observations. This computational bottleneck would be even more evident if using a Generalized Pareto response for analyzing peaks-over-threshold data. While including a nugget term as in [Zhang et al. \(2021\)](#) would alleviate much of the computation, it still adds an additional layer of numerical integration to the marginal transformation, which is already not in closed form.

Finally, while many of the key features of our proposed model are also found in recent “single-site conditioning” models ([Wadsworth and Tawn, 2022](#)), to our knowledge, ours is the first fully-specified joint model to possess them. In some ways, our model can be seen as an alternative to [Wadsworth and Tawn \(2022\)](#)-type models. These single-site conditioning models are more parsimonious and faster to fit than what we have proposed here. However, that our model is a well-defined joint probability model gives it significant advantages in both interpretability and applicability.

References

- Leonard Breiman. On some limit theorems similar to the arc-sin law. *Theory of Probability & Its Applications*, 10(2):323–331, 1965.
- Daniela Castro-Camilo and Raphaël Huser. Local likelihood estimation of complex tail dependence structures, applied to us precipitation extremes. *Journal of the American Statistical Association*, 115(531):1037–1054, 2020.
- Daren BH Cline. Convolution tails, product tails and domains of attraction. *Probability Theory and Related Fields*, 72(4):529–557, 1986.
- Daniel Cooley and Emeric Thibaud. Decompositions of dependence for high-dimensional extremes. *Biometrika*, 106(3):587–604, 2019.
- Lisandro Dalcin and Yao-Lung L. Fang. mpi4py: Status update after 12 years of development. *Computing in Science & Engineering*, 23(4):47–54, 2021. doi: 10.1109/MCSE.2021.3083216.

- A. C. Davison, R. Huser, and E. Thibaud. Geostatistics of Dependent and Asymptotically Independent Extremes. *Mathematical Geosciences*, 45(5):511–529, 2013. ISSN 1874-8953.
- Sebastian Engelke, Thomas Opitz, and Jennifer Wadsworth. Extremal dependence of random scale constructions. *Extremes*, 22(4):623–666, 2019.
- Christopher B Field, Vicente R Barros, Michael D Mastrandrea, Katharine J Mach, MA-K Abdabo, N Adger, Yury A Anokhin, Oleg A Anisimov, Douglas J Arent, Jonathon Barnett, et al. Summary for policymakers. In *Climate change 2014: impacts, adaptation, and vulnerability. Part A: global and sectoral aspects. Contribution of Working Group II to the Fifth Assessment Report of the Intergovernmental Panel on Climate Change*, pages 1–32. Cambridge University Press, Cambridge, United Kingdom and New York, NY, USA, 2014. doi: 10.1017/CBO9781107415379.
- Brian Gough. *GNU scientific library reference manual*. Network Theory Ltd., 2009.
- Arnab Hazra, Raphaël Huser, and David Bolin. Efficient modeling of spatial extremes over large geographical domains. *Journal of Computational and Graphical Statistics*, 2024.
- Janet Heffernan and Sidney Resnick. Hidden regular variation and the rank transform. *Advances in Applied Probability*, 37(2):393–414, 2005.
- Raphaël Huser and Marc G Genton. Non-stationary dependence structures for spatial extremes. *Journal of agricultural, biological, and environmental statistics*, 21(3):470–491, 2016.
- Raphaël Huser and Jennifer L Wadsworth. Modeling spatial processes with unknown extremal dependence class. *Journal of the American Statistical Association*, 114(525):434–444, 2019.
- Raphaël Huser, Thomas Opitz, and Emeric Thibaud. Bridging asymptotic independence and dependence in spatial extremes using gaussian scale mixtures. *Spatial Statistics*, 21:166–186, 2017.
- Raphaël Huser and Jennifer L. Wadsworth. Advances in statistical modeling of spatial extremes. *WIREs Computational Statistics*, 14(1):e1537, 2022. ISSN 1939-0068. doi: 10.1002/wics.1537.
- Anthony W Ledford and Jonathan A Tawn. Statistics for near independence in multivariate extreme values. *Biometrika*, 83(1):169–187, 1996.
- Leo R Belzile. *mev: Modelling of Extreme Values*, 2023. URL <https://lbelzile.github.io/mev/>.

- Reetam Majumder, Brian J Reich, and Benjamin A Shaby. Modeling extremal streamflow using deep learning approximations and a flexible spatial process. *The Annals of Applied Statistics*, 18(2):1519–1542, 2024.
- Matthew J. Menne, Imke Durre, Bryant Korzeniewski, Shelley McNeal, Kristy Thomas, Xungang Yin, Steven Anthony, Ron Ray, Russell S. Vose, Byron E. Gleason, and Tamara G. Houston. Global Historical Climatology Network - Daily (GHCN-Daily), Version 3. NOAA National Climatic Data Center (accessed 19 March 2018), 2012a.
- Matthew J Menne, Imke Durre, Russell S Vose, Byron E Gleason, and Tamara G Houston. An overview of the Global Historical Climatology Network-daily database. *Journal of Atmospheric and Oceanic Technology*, 29(7):897–910, 2012b.
- Paul CD Milly, Julio Betancourt, Malin Falkenmark, Robert M Hirsch, Zbigniew W Kundzewicz, Dennis P Lettenmaier, and Ronald J Stouffer. Stationarity is dead: Whither water management? *Science*, 319(5863):573–574, 2008. doi: 10.1126/science.1151915.
- John P Nolan. *Univariate Stable Distributions: Models for Heavy Tailed Data*. Springer Nature, 2020.
- Christopher J Paciorek and Mark J Schervish. Spatial modelling using a new class of nonstationary covariance functions. *Environmetrics: The official journal of the International Environmetrics Society*, 17(5):483–506, 2006.
- Anthony G Pakes. Convolution equivalence and infinite divisibility. *Journal of Applied Probability*, pages 407–424, 2004.
- Sidney I Resnick. *Extreme values, regular variation and point processes*. Springer, 2008.
- Mark D Risser and Catherine A Calder. Regression-based covariance functions for nonstationary spatial modeling. *Environmetrics*, 26(4):284–297, 2015.
- Mark D Risser, Christopher J Paciorek, Michael F Wehner, Travis A O’Brien, and William D Collins. A probabilistic gridded product for daily precipitation extremes over the united states. *Climate Dynamics*, 53(5):2517–2538, 2019.

- Benjamin Shaby and Martin T Wells. Exploring an adaptive metropolis algorithm. *Currently under review*, 1(1):17, 2010.
- Aldo V Vecchia. Estimation and model identification for continuous spatial processes. *Journal of the Royal Statistical Society Series B: Statistical Methodology*, 50(2):297–312, 1988.
- JL Wadsworth and JA Tawn. Higher-dimensional spatial extremes via single-site conditioning. *Spatial Statistics*, 51:100677, 2022.
- Holger Wendland. Piecewise polynomial, positive definite and compactly supported radial functions of minimal degree. *Advances in Computational Mathematics*, 4(1):389–396, December 1995.
- Likun Zhang, Benjamin A Shaby, and Jennifer L Wadsworth. Hierarchical transformed scale mixtures for flexible modeling of spatial extremes on datasets with many locations. *Journal of the American Statistical Association*, pages 1–13, 2021.
- Likun Zhang, Mark D Risser, Edward M Molter, Michael F Wehner, and Travis A O’Brien. Accounting for the spatial structure of weather systems in detected changes in precipitation extremes. *Weather and Climate Extremes*, 38:100499, 2022.
- Likun Zhang, Mark D. Risser, Michael F. Wehner, and Travis A. O’Brien. Leveraging extremal dependence to better characterize the 2021 pacific northwest heatwave. *Journal of Agricultural, Biological and Environmental Statistics*, June 2024. ISSN 1537-2693.
- Vladimir M Zolotarev. *One-dimensional stable distributions*, volume 65. American Mathematical Soc., 1986.

Appendix

A Technical proofs

A.1 Properties of stable distribution

The Stable distribution is important in both theory and application because it is the generalized central limit of random variables without second (or even first) order moments. Assume $S \sim \text{Stable}(\alpha, \beta, \gamma, \delta)$ under the 1-parameterization (Nolan, 2020) where $\alpha \in (0, 2]$ is the concentration parameter, $\beta \in [-1, 1]$ is the skewness parameter, $\gamma > 0$ is the scale parameter and $\delta \in \mathbb{R}$ is the location parameter. Then S has the characteristic function

$$E \exp(iuS) = \exp[-\gamma^\alpha |u|^\alpha \{1 - i\beta\omega(u)\text{sign}(u)\} + i\delta u], \quad u \in \mathbb{R},$$

where $\text{sign}(u)$ is the sign of u and $\omega(u) = \tan(\pi\alpha/2)\mathbb{1}(\alpha \neq 1) - 2\pi^{-1} \log |u|\mathbb{1}(\alpha = 1)$. If $\alpha < 1$ and $\beta = 1$, S has support $[\delta, \infty]$. Moreover, if $\alpha < 2$ and $0 < \beta \leq 1$, the tail of S is Pareto-like and satisfies $\Pr(S > x) \sim \gamma^\alpha (1 + \beta) C_\alpha x^{-\alpha}$ with $C_\alpha = \Gamma(\alpha) \sin(\alpha\pi/2)/\pi$ as $x \rightarrow \infty$.

More importantly, the Stable distributions are closed under convolution; sums of α -Stable variables (Stable variables with concentration parameter α) are still α -Stable. If $S_k \stackrel{\text{indep}}{\sim} \text{Stable}(\alpha, \beta_k, \gamma_k, \delta_k)$ and constant $w_k \geq 0$ for $k = 1, \dots, K$, then

$$\sum_{k=1}^K w_k S_k \sim \text{Stable}(\alpha, \bar{\beta}, \bar{\gamma}, \bar{\delta}) \tag{16}$$

with $\bar{\gamma} = \{\sum_{k=1}^K (w_k \gamma_k)^\alpha\}^{1/\alpha}$, $\bar{\beta} = \sum_{k=1}^K \beta_k (w_k \gamma_k)^\alpha / \bar{\gamma}^\alpha$ and $\bar{\delta} = \sum_{k=1}^K w_k \delta_k$.

To be able to examine the joint distribution of (X_i, X_j) for model (5), it is desirable for the mixture to have the same distributional support and rate of tail decay as each S_k . Thus in (7), we fixed $\beta_k \equiv 1$, $\delta_k \equiv \delta$ while imposing the constraint $\sum_{k=1}^K w_k = 1$. As a result, $\bar{\beta} = 1$ and $\bar{\delta} = \delta$, which means the univariate support of the $\{R(\mathbf{s})\}$ is $[\delta, \infty)$ everywhere. In consequence, we have $\Pr(R(\mathbf{s}) > x) \sim 2\bar{\gamma}^\alpha(\mathbf{s}) C_\alpha x^{-\alpha}$ for all $\mathbf{s} \in \mathcal{S}$ as $x \rightarrow \infty$ with $\bar{\gamma}(\mathbf{s}) = [\sum_{k=1}^K \{w_k(\mathbf{s}, r_k) \gamma_k\}^\alpha]^{1/\alpha}$, which means the process $\{R(\mathbf{s})\}$ has tail-stationarity.

A.2 Proof of Proposition 2.1

We begin by recalling a couple of useful theoretical results.

Lemma A.1 (Breiman (1965)). Assume X_1 and X_2 are two independent random variables that are both supported by \mathbb{R}^+ , and that $\Pr(X_1 > x) \in RV_{-\alpha}$, $\alpha \geq 0$.

(a) If there exists $\epsilon > 0$ such that $E(X_2^{\alpha+\epsilon}) < \infty$, then

$$\Pr(X_1 X_2 > x) \sim E(X_2^\alpha) \Pr(X_1 > x). \quad (17)$$

(b) Under the assumptions of part ((a)), we have

$$\sup_{x \geq y} \left| \frac{\Pr(X_1 X_2 > x)}{\Pr(X_1 > x)} - E(X_2^\alpha) \right| \rightarrow 0, \quad y \rightarrow \infty.$$

(c) If $\Pr(X_1 > x) \sim cx^{-\alpha}$, (17) holds under $E(X_2^\alpha) < \infty$.

(d) If $\Pr(X_2 > x) = o(\Pr(X_1 X_2 > x))$, then $\Pr(X_1 X_2 > x) \in RV_{-\alpha}$.

Lemma A.2 (Theorem 4(v) of [Cline \(1986\)](#)). Let $X_1 \sim F_1$ and $X_2 \sim F_2$ be two random variables that are both exponential tailed with the same rate, i.e. $F_i \in \text{ET}_{\alpha, \beta_i}$, $\alpha > 0$, $\beta_i > -1$, $i = 1, 2$.

Then

$$\Pr(X_1 + X_2 > x) \sim \alpha \frac{\Gamma(\beta_1 + 1) \Gamma(\beta_2 + 1)}{\Gamma(\beta_1 + \beta_2 + 1)} l(x) x^{\beta_1 + \beta_2 + 1} \exp(-\alpha x),$$

where $l(\cdot)$ is slowly varying.

Proof of Proposition 2.1. When $0 < \phi_j < \alpha$, the ϕ_j th moment of R_j exists: $E(R_j^{\phi_j}) < \infty$. This is sometimes called the fractional lower order moment. Recall that marginally $\Pr(W_j > x) = x^{-1}$.

Thus applying Lemma A.1 part (c) to $R_j W_j$ yields $\Pr(R_j^{\phi_j} W_j > x) = E(R_j^{\phi_j}) x^{-1}$.

When $\phi_j > \alpha$, $E(R_j^{\phi_j}) = \infty$. However, the tail of R_j is still regularly varying:

$$\Pr(R_j^{\phi_j} > x) \sim 2C_\alpha \bar{\gamma}_j^\alpha x^{-\frac{\alpha}{\phi_j}}$$

and

$$E\left(W_j^{\frac{\alpha}{\phi_j}}\right) = \int_1^\infty w^{\frac{\alpha}{\phi_j} - 2} dw = \frac{1}{1 - \alpha/\phi_j}.$$

From Lemma A.1(c),

$$\Pr(R_j^{\phi_j} W_j > x) \sim E\left(W_j^{\frac{\alpha}{\phi_j}}\right) \Pr(R_j^{\phi_j} > x),$$

from which the result follows.

When $\phi_j = \alpha$, $R_j^{\phi_j}$ and W_j are regularly varying with the same index -1 . Therefore, $\log R_j^{\phi_j}$ and $\log W_j$ are both in $ET_{1,0}$. By Lemma A.2,

$$\Pr(R_j^{\phi_j} W_j > x) \sim 2C_\alpha \bar{\gamma}_j^\alpha x^{-1} \log x.$$

□

Remark 4. By Theorem 3.8 and Lemma 3.12 of [Nolan \(2020\)](#), we can write out the exact form of the fractional lower order moment of $R_j \sim \text{Stable}(\alpha, 1, \bar{\gamma}_j, \delta)$ if $\delta = 0$:

$$E(R_j^{\phi_j}) = \bar{\gamma}_j^{\phi_j} \cos^{-\frac{\phi_j}{\alpha}}\left(\frac{\pi\alpha}{2}\right) \frac{\Gamma(1 - \phi_j/\alpha)}{\Gamma(1 - \phi_j)}.$$

A.3 Limiting angular measure for linear combinations of independent stable variables

Consider

$$\begin{aligned} R_1 &= w_{11}S_1 + \dots + w_{K1}S_K, \\ R_2 &= w_{12}S_1 + \dots + w_{K2}S_K, \\ &\vdots \\ R_m &= w_{1m}S_1 + \dots + w_{Km}S_K, \end{aligned}$$

with deterministic coefficient vectors $\mathbf{w}_i = (w_{1i}, \dots, w_{Ki})^\top$, $i = 1, \dots, m$. The random vector $\mathbf{S} = (S_1, \dots, S_K)^\top$ is composed of regularly varying variables. In matrix notation, we write $\Psi = (\mathbf{w}_1, \dots, \mathbf{w}_m)^\top \in \mathbb{R}^{m \times K}$ and

$$(R_1, \dots, R_m)^\top = \Psi \mathbf{S}.$$

To show Proposition 2.2, we first slightly reformulate Corollary 1 of Cooley and Thibaud (2019) where we consider only non-negative weights in Ψ .

Lemma A.3 (Cooley and Thibaud, 2019). Assume the independently and identically distributed random variables \tilde{S}_k , $k = 1, \dots, K$ are regularly varying at infinity, i.e.,

$$n \Pr(\tilde{S}_k/b_n > x) \rightarrow x^{-\alpha}, \quad n \rightarrow \infty, \quad (18)$$

where $b_n > 0$ and $\alpha > 0$. Also, the normalizing sequence $b_n \rightarrow \infty$, and Ψ is a matrix with m rows, K columns and has only non-negative entries and at least one positive entry. Then the random vector $\Psi \tilde{\mathbf{S}}$ is regularly varying at infinity with tail index α and it has angular measure (in dimension K and with respect to any chosen norm $\|\cdot\|$) given by

$$H_{\Psi \tilde{\mathbf{S}}}(\cdot) = \sum_{k=1}^K \|\omega_k\|^\alpha \times \delta_{\omega_k/\|\omega_k\|}(\cdot), \quad (19)$$

where δ is the Dirac mass function, and we set the sum term for k to 0 if $\|\omega_k\| = 0$.

Since $\Psi \tilde{\mathbf{S}}$ exhibits regularly variation, the scaling property holds for a given norm $\|\cdot\|$. Define the unit ball $\mathbb{S}_{m-1}^+ = \{\mathbf{x} \in \mathbb{R}_+^m : \|\mathbf{x}\| = 1\}$. For a set $C(r, B) = \{\mathbf{x} \in \mathbb{R}_+^m : \|\mathbf{x}\| > r, \|\mathbf{x}\|^{-1}\mathbf{x} \in B\}$ with $r > 0$ and $B \subset \mathbb{S}_{m-1}^+$ being a Borel set. Then we have

$$n \Pr(b_n^{-1} \Psi \tilde{\mathbf{S}} \in C(r, B)) \sim r^{-\alpha} H_{\Psi \tilde{\mathbf{S}}}(B), \quad \text{as } n \rightarrow \infty.$$

If we let $B = \mathbb{S}_{m-1}^+$, the event $b_n^{-1} \Psi \tilde{\mathbf{S}} \in C(r, B)$ is equivalent to $\|\Psi \tilde{\mathbf{S}}\|/b_n > r$. Also note that the angular measure $H_{\Psi \tilde{\mathbf{S}}}$ is usually not a probability measure since its total measure is

$$m_{\Psi\tilde{\mathbf{S}}} = H_{\Psi\tilde{\mathbf{S}}}(\mathbb{S}_{m-1}^+) = \sum_{k=1}^K \|\boldsymbol{\omega}_k\|^\alpha. \text{ Therefore,}$$

$$n \Pr\left(\|\Psi\tilde{\mathbf{S}}\|/b_n > r\right) \sim m_{\Psi\tilde{\mathbf{S}}} r^{-\alpha}, \text{ as } n \rightarrow \infty. \quad (20)$$

Using this result, marginal and joint upper tail behaviour of $(R_1, \dots, R_m)^\top$ can be derived when the coefficients in \mathbf{S}_t are regularly varying. Proposition 2.2 constitutes a special case, focusing on two linear combinations of stable distributions, which are a specific example of regularly varying random variables.

Proof of Proposition 2.2. (a) The case of $\mathcal{C}_i \cap \mathcal{C}_j = \emptyset$ is clear because independence holds and individually $\Pr(R_i > x) \sim 2\bar{\gamma}_i^\alpha C_\alpha x^{-\alpha}$ and $\Pr(R_j > x) \sim 2\bar{\gamma}_j^\alpha C_\alpha x^{-\alpha}$.

When $\mathcal{C}_i \cap \mathcal{C}_j = \emptyset$, we show Expression (11) by applying Lemma A.3. First we notice that the upper tails of the stable distributions with the same concentration α and skewness $\beta = 1$ are equivalent up to a positive scaling constant. More specifically, we denote $\tilde{S}_k = S_k/\gamma_k$, $k = 1, \dots, K$, and then all \tilde{S}_k 's are iid $\text{Stable}(\alpha, 1, 1, \delta)$ variables because the S_k 's share the location δ in Equation (7).

Therefore, Lemma A.3 is applicable for the pair $(R_i, R_j)^\top$ under the new weights $(w_{1i}\gamma_1, \dots, w_{Ki}\gamma_K)^\top$ and $(w_{1j}\gamma_1, \dots, w_{Kj}\gamma_K)^\top$. Since $\Pr(\tilde{S}_k > x) \sim 2C_\alpha x^{-\alpha}$ as $x \rightarrow \infty$, we can therefore choose

$$b_n = (2nC_\alpha)^{1/\alpha}$$

so $n\Pr(\tilde{S}_k/b_n > x) \rightarrow x^{-\alpha}$ as $n \rightarrow \infty$. Choosing the componentwise min-operator as the norm, Expression (20) can be re-written as:

$$n\Pr(\min(R_i, R_j)/b_n > r) \sim r^{-\alpha} \sum_{k=1}^K \min(w_{ki}\gamma_k, w_{kj}\gamma_k)^\alpha = r^{-\alpha} \sum_{k=1}^K w_{k,\wedge}^\alpha \gamma_k^\alpha,$$

in which $w_{k,\wedge} = \min(w_{ki}, w_{kj})$. The previous display immediately induces Equation (11).

(b) We only prove the inequality concerning $\min(c_i R_i^{\phi_i}, c_j R_j^{\phi_j})$. The proof for $\max(c_i R_i^{\phi_i}, c_j R_j^{\phi_j})$ is analogous.

If $\mathcal{C}_i = \mathcal{C}_j$, R_i and R_j share the same non-zero indices. Since $1/\phi_i - 1/\phi_j > 0$, $c_i^{1/\phi_i} w_{ki}/x^{1/\phi_i - 1/\phi_j} < c_j^{1/\phi_j} w_{kj}$, $k = 1, \dots, K$ for sufficiently large x . Therefore

$$\begin{aligned} \Pr\{\min(c_i R_i^{\phi_i}, c_j R_j^{\phi_j}) > x\} &= P\left(\frac{c_i^{1/\phi_i}}{x^{1/\phi_i - 1/\phi_j}} R_i > x^{1/\phi_j}, c_j^{1/\phi_j} R_j > x^{1/\phi_j}\right) \\ &= P\left(\frac{c_i^{1/\phi_i}}{x^{1/\phi_i - 1/\phi_j}} R_i > x^{1/\phi_j}\right) \sim 2C_\alpha \sum_{k \in \mathcal{C}_i} (w_{ki}\gamma_k)^\alpha c_i^{\alpha/\phi_i} x^{-\alpha/\phi_i}. \end{aligned}$$

If either $\mathcal{C}_i \setminus \mathcal{C}_j$ or $\mathcal{C}_j \setminus \mathcal{C}_i$ is non-empty, we define

$$R_{i,\setminus} = \sum_{k \in \mathcal{C}_i \setminus \mathcal{C}_j} w_{ki} S_k, \quad R_{i,\cap} = \sum_{k \in \mathcal{C}_i \cap \mathcal{C}_j} w_{ki} S_k, \quad (21)$$

and $R_i = R_{i,\setminus} + R_{i,\cap}$. Similarly we define $R_{j,\setminus}$ and $R_{j,\cap}$. Then the classic c_r -inequality gives us $R_{i,\cap}^{\phi_i} \leq R_i^{\phi_i} \leq 2^{\phi_i}(R_{i,\cap}^{\phi_i} + R_{i,\setminus}^{\phi_i})$. Similarly, it is also true that $R_{j,\cap}^{\phi_j} \leq R_j^{\phi_j} \leq 2^{\phi_j}(R_{j,\cap}^{\phi_j} + R_{j,\setminus}^{\phi_j})$.

Therefore,

$$\begin{aligned} \Pr\{\min(c_i R_{i,\cap}^{\phi_i}, c_j R_{j,\cap}^{\phi_j}) > x\} &\leq P\{\min(c_i R_i^{\phi_i}, c_j R_j^{\phi_j}) > x\} \leq \\ &P\{2^{\phi_i} c_i (R_{i,\cap}^{\phi_i} + R_{i,\setminus}^{\phi_i}) > x, 2^{\phi_j} c_j (R_{j,\cap}^{\phi_j} + R_{j,\setminus}^{\phi_j}) > x\}. \end{aligned} \quad (22)$$

The lower bound in (22) can be approximated using the first case $\mathcal{C}_i = \mathcal{C}_j$. The upper bound in

(22) can be further bounded by $\Pr(\min(2^{\phi_i} c_i R_{i,\cap}^{\phi_i}, 2^{\phi_j} c_j R_{j,\cap}^{\phi_j}) + \max(2^{\phi_i} c_i R_{i,\setminus}^{\phi_i}, 2^{\phi_j} c_j R_{j,\setminus}^{\phi_j}) > x)$,

which can be approximated using Lemma A.4 because

$$\begin{aligned} \Pr\{\min(2^{\phi_i} c_i R_{i,\cap}^{\phi_i}, 2^{\phi_j} c_j R_{j,\cap}^{\phi_j}) > x\} &\sim 2C_\alpha \sum_{k \in \mathcal{C}_i \cap \mathcal{C}_j} (w_{ki} \gamma_k)^\alpha c_i^{\alpha/\phi_i} x^{-\alpha/\phi_i}, \\ \Pr\{\max(2^{\phi_i} c_i R_{i,\setminus}^{\phi_i}, 2^{\phi_j} c_j R_{j,\setminus}^{\phi_j}) > x\} &\sim 2^{\alpha+1} C_\alpha \sum_{k \in \mathcal{C}_i \setminus \mathcal{C}_j} (w_{ki} \gamma_k)^\alpha c_i^{\alpha/\phi_i} x^{-\alpha/\phi_i}. \end{aligned}$$

The second inequality holds due to the independence between $R_{i,\setminus}$ and $R_{j,\setminus}$. Combining the approximations of the two bounds yields the stated range of the constant d_\wedge .

□

A.4 Proof of Theorem 2.3

To examine the joint tail of (R_i, R_j) and (X_i, X_j) , we begin by recalling the useful results from the literature. The first result is an easy but useful inequality

$$\begin{aligned} \Pr(\min(R_1, R_2) + \min(W_1, W_2) > x) &\leq \Pr(R_1 + W_1 > x, R_2 + W_2 > x) \leq \\ &\Pr(\min(R_1, R_2) + \max(W_1, W_2) > x). \end{aligned} \quad (23)$$

The second relates to the tail behaviour on the convolution with a CE_α distribution.

Lemma A.4 (Theorem 1 of Cline (1986) and Lemma 5.1 of Pakes (2004)). Let $Y_1 \sim F_1$ and $Y_2 \sim F_2$ be random variables. If distribution function $F_1 \in CE_\alpha$ with $\alpha \geq 0$ and $E(e^{\alpha Y_2}) < \infty$ while $\Pr(Y_2 > x)/\Pr(Y_1 > x) \rightarrow c \geq 0$ as $x \rightarrow \infty$, then

$$\Pr(Y_1 + Y_2 > x)/\Pr(Y_1 > x) \rightarrow E(e^{\alpha Y_2}) + cE(e^{\alpha Y_1}), \quad x \rightarrow \infty.$$

Lemma A.5 (Proposition 5 in Engelke et al. (2019)). Suppose $\bar{F}_W \in RV_{-\alpha_W}$ with $\alpha_W \geq 0$, and $\bar{F}_R \in RV_{-\alpha_R}$ with $\alpha_R > \alpha_W$. Let $R \sim F_R$ and $(W_1, W_2) \stackrel{d}{=} F_W$ marginally while $R \perp\!\!\!\perp (W_1, W_2)$. Denote $(X_1, X_2) = R(W_1, W_2)$. If the extremal dependence of (W_1, W_2) is summarized by (χ_W, η_W) ,

then $\chi_X = \chi_W$ and

$$\eta_X = \begin{cases} \alpha_W/\alpha_R, & \text{if } \alpha_R < \alpha_W/\eta_W, \\ \eta_W, & \text{if } \alpha_R > \alpha_W/\eta_W. \end{cases}$$

Proof of Theorem 2.3. (a) Since $\phi_i > \alpha$ and $\phi_j > \alpha$, (10) ensures

$$F_{X_i}^{-1}(1-q) \sim \{(1-\alpha/\phi_i)\theta_i\}^{-\phi_i/\alpha} q^{-\phi_i/\alpha} \text{ with } \theta_i = \frac{1}{2C_\alpha \bar{\gamma}_i^\alpha} > 0.$$

Similar result holds for $F_{X_j}^{-1}(1-q)$. Therefore

$$\begin{aligned} & P(X_i \geq F_{X_i}^{-1}(1-q), X_j \geq F_{X_j}^{-1}(1-q)) \\ &= P\left(R_i^{\phi_i} W_i > \{(1-\alpha/\phi_i)\theta_i\}^{-\phi_i/\alpha} q^{-\phi_i/\alpha}, R_j^{\phi_j} W_j > \{(1-\alpha/\phi_j)\theta_j\}^{-\phi_j/\alpha} q^{-\phi_j/\alpha}\right) \\ &= P\left(\theta_i R_i^\alpha \frac{W_i^{\alpha/\phi_i}}{E(W_i^{\alpha/\phi_i})} > q^{-1}, \theta_j R_j^\alpha \frac{W_j^{\alpha/\phi_j}}{E(W_j^{\alpha/\phi_j})} > q^{-1}\right). \end{aligned} \quad (24)$$

Using Expression (23) and Lemma A.1 part (c) again, we deduce that that the right-hand side of (24) is bounded with the range

$$E\left\{\min\left(\frac{W_i^{\alpha/\phi_i}}{E(W_i^{\alpha/\phi_i})}, \frac{W_j^{\alpha/\phi_j}}{E(W_j^{\alpha/\phi_j})}\right)\right\} \left[\Pr(\min(\theta_i R_i^\alpha, \theta_j R_j^\alpha) > q^{-1}), \Pr(\max(\theta_i R_i^\alpha, \theta_j R_j^\alpha) > q^{-1})\right].$$

Meanwhile, we know from Proposition 2.2(a) that

$$\begin{aligned} \Pr(\min(\theta_i R_i^\alpha, \theta_j R_j^\alpha) > q^{-1}) &= \Pr(\theta_i^{1/\alpha} R_i > q^{-1/\alpha}, \theta_j^{1/\alpha} R_j > q^{-1/\alpha}) \\ &= 2C_\alpha C_K(\theta_i^{1/\alpha} \mathbf{w}_i, \theta_j^{1/\alpha} \mathbf{w}_j, \gamma)q, \end{aligned} \quad (25)$$

in which

$$\begin{aligned} C_K(\theta_i^{1/\alpha} \mathbf{w}_i, \theta_j^{1/\alpha} \mathbf{w}_j, \gamma) &= \sum_{k=1}^K \min\{\theta_i \gamma_k^\alpha w_{ki}^\alpha, \theta_j \gamma_k^\alpha w_{kj}^\alpha\} = \frac{1}{2C_\alpha} \sum_{k=1}^K \min\left\{\frac{\gamma_k^\alpha w_{ki}^\alpha}{\bar{\gamma}_i^\alpha}, \frac{\gamma_k^\alpha w_{kj}^\alpha}{\bar{\gamma}_j^\alpha}\right\} \\ &= \frac{1}{2C_\alpha} \sum_{k=1}^K \min\left\{\frac{(w_{ki} \gamma_k)^\alpha}{\sum_{k \in \mathcal{C}_i} (w_{ki} \gamma_k)^\alpha}, \frac{(w_{kj} \gamma_k)^\alpha}{\sum_{k \in \mathcal{C}_j} (w_{kj} \gamma_k)^\alpha}\right\} = \frac{1}{2C_\alpha} \sum_{\mathcal{C}_i \cap \mathcal{C}_j} v_{k,\wedge}. \end{aligned}$$

On the other hand,

$$\begin{aligned} \Pr(\max(\theta_i R_i^\alpha, \theta_j R_j^\alpha) > q^{-1}) &= 1 - \Pr(\max(\theta_i R_i^\alpha, \theta_j R_j^\alpha) \leq q^{-1}) \\ &= \Pr(\theta_i R_i^\alpha > q^{-1}, \theta_j R_j^\alpha < q^{-1}) + \Pr(\theta_i R_i^\alpha < q^{-1}, \theta_j R_j^\alpha > q^{-1}) + \\ &\quad \Pr(\theta_i R_i^\alpha > q^{-1}, \theta_j R_j^\alpha > q^{-1}), \end{aligned}$$

By Proposition 2.2(a) and Expression (25), the previous display becomes

$$\Pr(\max(\theta_i R_i^\alpha, \theta_j R_j^\alpha) > q^{-1}) = 2C_\alpha C_K(\theta_i^{1/\alpha} \mathbf{w}_i, \theta_j^{1/\alpha} \mathbf{w}_j, \gamma)q + o(q).$$

Therefore, both $\Pr(\min(\theta_i R_i^\alpha, \theta_j R_j^\alpha) > q^{-1})$ and $\Pr(\max(\theta_i R_i^\alpha, \theta_j R_j^\alpha) > q^{-1})$ are dominated by $2C_\alpha C_K(\theta_i^{1/\alpha} \mathbf{w}_i, \theta_j^{1/\alpha} \mathbf{w}_j, \gamma)q$. Consequently, we get $\eta_X = 1$ and

$$\chi_{ij} = E\left\{\min\left(\frac{W_i^{\alpha/\phi_i}}{E(W_i^{\alpha/\phi_i})}, \frac{W_j^{\alpha/\phi_j}}{E(W_j^{\alpha/\phi_j})}\right)\right\} \sum_{k=1}^K v_{k,\wedge}.$$

(b) When $0 < \phi_i < \phi_j < \alpha$, write $\lambda_i = E(R_i^{\phi_i})$ and $\lambda_j = E(R_j^{\phi_j})$. By (10),

$$F_{X_i}^{-1}(1-q) \sim \lambda_i q^{-1}, \quad F_{X_j}^{-1}(1-q) \sim \lambda_j q^{-1},$$

and

$$\Pr(X_i \geq F_{X_i}^{-1}(1-q), X_j \geq F_{X_j}^{-1}(1-q)) = P \left(\frac{R_i^{\phi_i}}{\lambda_i} W_i > q^{-1}, \frac{R_j^{\phi_j}}{\lambda_j} W_j > q^{-1} \right).$$

If $\phi_i/\alpha < \phi_j/\alpha < \eta_W$, we first regard $R^* = \max(R_i^{\phi_i}/\lambda_i, R_j^{\phi_j}/\lambda_j)$ as a radial variable. From Proposition 2.2(b), we have $\Pr(R^* > x) \in RV_{-\alpha/\phi_j}$ and $\alpha_{R^*} = \alpha/\phi_j > \alpha_W = 1$. Since $\alpha/\phi_j > 1/\eta_W$, we know from Lemma A.5 that

$$\lim_{q \rightarrow 0} \frac{\log \Pr(R^* W_i > q^{-1}, R^* W_j > q^{-1})}{\log \Pr(R^* W_i > q^{-1})} = \eta_W.$$

Then we regard $R_* = \min(R_i^{\phi_i}/\lambda_i, R_j^{\phi_j}/\lambda_j)$ as a radial variable. Since $\alpha_{R_*} = \alpha/\phi_i > 1/\eta_W$, Lemma A.5 again gives

$$\lim_{q \rightarrow 0} \frac{\log \Pr(R_* W_i > q^{-1}, R_* W_j > q^{-1})}{\log \Pr(R_* W_i > q^{-1})} = \eta_W. \quad (26)$$

Moreover, $E(R^*) < \infty$ and $E(R_*) < \infty$ due to $\phi_i < \phi_j < \alpha$. We can apply Lemma A.1 part (c) again to show $\log \Pr(R^* W_i > q^{-1}) \sim \log \Pr(R_* W_i > q^{-1}) \sim \log \Pr(R_i^{\phi_i} W_i > \lambda_i q^{-1})$. By sandwich limit theorem and (23),

$$\eta_X = \lim_{q \rightarrow 0} \frac{\log \Pr(R_i^{\phi_i} W_i > \lambda_i q^{-1}, R_i^{\phi_i} W_j > \lambda_i q^{-1})}{\log \Pr(R_i^{\phi_i} W_i > \lambda_i q^{-1})} = \eta_W,$$

and $\chi_X = \chi_W = 0$.

If $\eta_W < \phi_i/\alpha < \phi_j/\alpha$, we have $\alpha/\phi_j < \alpha/\phi_i < 1/\eta_W$. Lemma A.5 ensures

$$\lim_{q \rightarrow 0} \frac{\log \Pr(R^* W_i > q^{-1}, R^* W_j > q^{-1})}{\log \Pr(R^* W_i > q^{-1})} = \alpha_W/\alpha_{R^*} = \phi_j/\alpha, \quad (27)$$

and

$$\lim_{q \rightarrow 0} \frac{\log \Pr(R_* W_i > q^{-1}, R_* W_j > q^{-1})}{\log \Pr(R_* W_i > q^{-1})} = \alpha_W/\alpha_{R_*} = \phi_i/\alpha.$$

Therefore, $\eta_X \in [\phi_i/\alpha, \phi_j/\alpha]$ and $\chi_X = \chi_W = 0$.

If $\phi_i/\alpha < \eta_W < \phi_j/\alpha$, we have $\alpha/\phi_j < 1/\eta_W < \alpha/\phi_i$. Therefore, (27) holds for R^* and (26) holds for R_* , which proves $\eta_X \in [\eta_W, \phi_j/\alpha]$ and $\chi_X = 0$.

(c) When $\phi_i < \alpha < \phi_j$, write $\lambda_i = E(R_i^{\phi_i})$ and $\psi_j = (1 - \alpha/\phi_j)/\{2C_\alpha \bar{\gamma}_i^\alpha\}$. By (10),

$$F_{X_i}^{-1}(1-q) \sim \lambda_i q^{-1}, \quad F_{X_j}^{-1}(1-q) \sim (\psi_j q)^{-\phi_j/\alpha}.$$

First, we assume $\mathbf{w}_i = \mathbf{w}_j$, i.e., $R_i = R_j$. Denote the distribution and density function of R_i

and R_j as F_R and f_R , and then

$$F_R = \text{Stable}(\alpha, 1, \bar{\gamma}, 0), \quad \bar{\gamma} = \left\{ \sum_{k \in \mathcal{C}_i} (w_{ki} \gamma_k)^\alpha \right\}^{\frac{1}{\alpha}}.$$

Thus,

$$\begin{aligned} \Pr(X_i \geq F_{X_i}^{-1}(1-q), X_j \geq F_{X_j}^{-1}(1-q)) &= \Pr(R_i^{\phi_i} W_i > \lambda_i q^{-1}, R_j^{\phi_j} W_j > (\psi_j q)^{-\phi_j/\alpha}) \\ &= \int_0^\infty P\left(r^{\phi_i} W_i > \lambda_i q^{-1}, r^{\phi_j} W_j > (\psi_j q)^{-\phi_j/\alpha}\right) f_R(r) dr. \end{aligned} \quad (28)$$

Since $q^{-1/\phi_j} > q^{-1/\alpha}$ for sufficiently small q , we can split the limits of the integral in (28) into $(0, (\theta_j^* q)^{-1/\alpha})$, $((\theta_j^* q)^{-1/\alpha}, (\lambda_i q^{-1})^{1/\phi_i})$, and $((\lambda_i q^{-1})^{1/\phi_i}, \infty)$.

(i) When $r \in ((\lambda_i q^{-1})^{1/\phi_i}, \infty)$, we have $\lambda_i q^{-1}/r^{\phi_i} < 1$ and $(\psi_j q)^{-\phi_j/\alpha}/r^{\phi_j} < 1$. Thus,

$$\begin{aligned} &\int_{(\lambda_i q^{-1})^{1/\phi_i}}^\infty P\left(r^{\phi_i} W_i > \lambda_i q^{-1}, r^{\phi_j} W_j > (\psi_j q)^{-\phi_j/\alpha}\right) f_R(r) dr \\ &= \Pr(R_i > (\lambda_i q^{-1})^{1/\phi_i}) \sim 2C_\alpha \bar{\gamma}^\alpha \lambda_i^{-\alpha/\phi_i} q^{\alpha/\phi_i}. \end{aligned} \quad (29)$$

(ii) When $r \in ((\theta_j^* q)^{-1/\alpha}, (\lambda_i q^{-1})^{1/\phi_i})$, $\lambda_i q^{-1}/r^{\phi_i} > 1$ and $(\psi_j q)^{-\phi_j/\alpha}/r^{\phi_j} < 1$. Thus,

$$\begin{aligned} &\int_{(\theta_j^* q)^{-1/\alpha}}^{(\lambda_i q^{-1})^{1/\phi_i}} P\left(r^{\phi_i} W_i > \lambda_i q^{-1}, r^{\phi_j} W_j > (\psi_j q)^{-\phi_j/\alpha}\right) f_R(r) dr \\ &= \int_{(\theta_j^* q)^{-1/\alpha}}^{(\lambda_i q^{-1})^{1/\phi_i}} \Pr(r^{\phi_i} W_i > \lambda_i q^{-1}) f_R(r) dr = \lambda_i^{-1} q \int_{(\theta_j^* q)^{-1/\alpha}}^{(\lambda_i q^{-1})^{1/\phi_i}} r^{\phi_i} f_R(r) dr \\ &= \lambda_i^{-1} q \int_{(\theta_j^* q)^{-1/\alpha}}^{(\lambda_i q^{-1})^{1/\phi_i}} \frac{1}{\pi \bar{\gamma}} \sum_{m=1}^\infty \frac{\Gamma(m\alpha + 1) \sin(m\pi\alpha) (-1)^{m+1}}{m!} \left(\cos \frac{\pi\alpha}{2}\right)^{-m} \frac{r^{\phi_i - m\alpha - 1}}{\bar{\gamma}^{-m\alpha - 1}} dr \\ &\sim 2\Gamma(\alpha) \sin(\pi\alpha/2) \bar{\gamma}^\alpha \frac{\lambda_i^{-1} \psi_j^{1-\phi_i/\alpha}}{\pi(1-\phi_i/\alpha)} q^{2-\phi_i/\alpha} = \frac{\lambda_i^{-1} \psi_j^{-\phi_i/\alpha} (1-\alpha/\phi_j)}{1-\phi_i/\alpha} q^{2-\phi_i/\alpha}. \end{aligned} \quad (30)$$

The penultimate line uses the series expansion for the stable density when $\alpha \neq 1$; see [Zolotarev \(1986, Chapter 2\)](#).

(iii) When $r \in (0, (\theta_j^* q)^{-1/\alpha})$, we have

$$\begin{aligned} &\int_0^{(\theta_j^* q)^{-1/\alpha}} P\left(r^{\phi_i} W_i > \lambda_i q^{-1}, r^{\phi_j} W_j > (\psi_j q)^{-\phi_j/\alpha}\right) f_R(r) dr \\ &\leq \int_0^{(\theta_j^* q)^{-1/\alpha}} \exp\left[-\frac{\log(\lambda_i q^{-1}/r^{\phi_i}) + \log\{(\psi_j q)^{-\phi_j/\alpha}/r^{\phi_j}\}}{1+\rho}\right] f_R(r) dr \\ &= (\psi_j^{-\phi_j/\alpha} \lambda_i)^{-1/(1+\rho)} q^{(1+\phi_j/\alpha)/(1+\rho)} \int_0^{(\theta_j^* q)^{-1/\alpha}} r^{(\phi_i+\phi_j)/(1+\rho)} f_R(r) dr. \end{aligned} \quad (31)$$

Note that $r^{(\phi_i+\phi_j)/(1+\rho)} f_R(r) \rightarrow 0$ as $r \rightarrow 0$, and $r^{(\phi_i+\phi_j)/(1+\rho)} f_R(r) \sim r^{(\phi_i+\phi_j)/(1+\rho)-\alpha-1}$ as $r \rightarrow \infty$. By Karamata's Theorem ([Resnick, 2008, p.17](#)), $\int_0^x r^{(\phi_i+\phi_j)/(1+\rho)} f_R(r) dr \in RV_{(\phi_i+\phi_j)/(1+\rho)-\alpha}$ when $(\phi_i+\phi_j)/(1+\rho) \geq \alpha$. When $(\phi_i+\phi_j)/(1+\rho) < \alpha$, $\int_0^x r^{(\phi_i+\phi_j)/(1+\rho)} f_R(r) dr <$

$E\{R_i^{(\phi_i+\phi_j)/(1+\rho)}\} < \infty$. Apply this result to the right-hand side of (31) to get

$$\begin{aligned} & \int_0^{(\theta_j^* q)^{-1/\alpha}} P\left(r^{\phi_i} W_i > \lambda_i q^{-1}, r^{\phi_j} W_j > (\psi_j q)^{-\phi_j/\alpha}\right) f_R(r) dr \\ & \leq \begin{cases} L_R(q^{-1}) q^{(1-\phi_i/\alpha)/(1+\rho)+1}, & \text{if } (\phi_i + \phi_j)/(2\eta_W) \geq \alpha, \\ C_R q^{(1+\phi_j/\alpha)/(1+\rho)}, & \text{if } (\phi_i + \phi_j)/(2\eta_W) < \alpha, \end{cases} \end{aligned}$$

where $L_R \in RV_0$ and $C_R = (\psi_j^{-\phi_j/\alpha} \lambda_i)^{-1/(1+\rho)} E\{R_i^{(\phi_i+\phi_j)/(1+\rho)}\}$.

On the other hand,

$$\begin{aligned} & \int_0^{(\theta_j^* q)^{-1/\alpha}} P\left(r^{\phi_i} W_i > \lambda_i q^{-1}, r^{\phi_j} W_j > (\psi_j q)^{-\phi_j/\alpha}\right) f_R(r) dr \\ & \geq \int_0^{(\theta_j^* q)^{-1/\alpha}} P\left(r^{\phi_i} W_i > \lambda_i q^{-1}\right) P\left(r^{\phi_j} W_j > (\psi_j q)^{-\phi_j/\alpha}\right) f_R(r) dr \quad (32) \\ & = \psi_j^{\phi_j/\alpha} \lambda_i^{-1} q^{1+\phi_j/\alpha} \int_0^{(\theta_j^* q)^{-1/\alpha}} r^{\phi_i+\phi_j} f_R(r) dr = \tilde{L}_R(q^{-1}) q^{2-\phi_i/\alpha}, \end{aligned}$$

in which $\tilde{L}_R \in RV_0$.

Combine the results from (29) - (32) under the assumption that $\mathbf{w}_i = \mathbf{w}_j$, and we can obtain lower and upper bounds of the regularly varying index for $\Pr(X_i \geq F_{X_i}^{-1}(1-q), X_j \geq F_{X_j}^{-1}(1-q))$, which is also known as η_X .

When $\mathbf{w}_i \neq \mathbf{w}_j$ and $\mathcal{C}_i \cap \mathcal{C}_j \neq \emptyset$,

$$\begin{aligned} & P\left[\left(\sum_k w_{k,\wedge} S_k\right)^{\phi_i} W_i > \lambda_i q^{-1}, \left(\sum_k w_{k,\wedge} S_k\right)^{\phi_j} W_j > (\psi_j q)^{-\phi_j/\alpha}\right] \\ & \leq \Pr(R_i^{\phi_i} W_i > \lambda_i q^{-1}, R_j^{\phi_j} W_j > (\psi_j q)^{-\phi_j/\alpha}) \\ & \leq P\left[\left(\sum_k w_{k,\vee} S_k\right)^{\phi_i} W_i > \lambda_i q^{-1}, \left(\sum_k w_{k,\vee} S_k\right)^{\phi_j} W_j > (\psi_j q)^{-\phi_j/\alpha}\right], \end{aligned}$$

whose bounds can be dealt with the results we just obtained while assuming $\mathbf{w}_i = \mathbf{w}_j$. Since the bounds for η_X did not depend on the weights, they stay the same for when $\mathbf{w}_i \neq \mathbf{w}_j$.

□

B MCMC details

Conditioning on the scaling variable \mathbf{S}_t at the knots, we define the hierarchical model as

$$\begin{aligned} \mathcal{L}(\mathbf{Y}_t | \boldsymbol{\theta}_{\mathbf{Y}_t}, \mathbf{S}_t, \boldsymbol{\gamma}, \boldsymbol{\phi}, \boldsymbol{\rho}) &= \varphi_D(\mathbf{Z}_t) \left| \frac{\partial \mathbf{Z}_t}{\partial \mathbf{Y}_t} \right| \\ \mathbf{S}_t | \boldsymbol{\gamma} &\sim \text{Stable}(\alpha = 0.5, 1, \boldsymbol{\gamma}, \delta = 0) \\ \phi_k &\stackrel{\text{iid}}{\sim} \text{Beta}(5, 5), \\ \rho_k &\stackrel{\text{iid}}{\sim} \text{halfNormal}(0, 2), \\ k &= 1, \dots, K \end{aligned}$$

in which φ_D is the D -variate Gaussian density function with covariance matrix $\boldsymbol{\Sigma}_\rho$ and $\partial \mathbf{Z}_t / \partial \mathbf{Y}_t$ is the Jacobian. Using the inverse function theorem that the derivative of $F^{-1}(t)$ is equal to $1/F'(F^{-1}(t))$ as long as $F'(F^{-1}(t)) \neq 0$, the Jacobian is a diagonal matrix with elements

$$\begin{aligned} \frac{\partial Z_{tj}}{\partial Y_{tj}} &= \frac{1}{\varphi \left\{ \Phi^{-1} \left(1 - \frac{1}{X_{tj}/R_{tj}^{\phi_j} + 1} \right) \right\}} \cdot \frac{1}{(X_{tj}/R_{tj}^{\phi_j} + 1)^2 R_{tj}^{\phi_j}} \cdot \frac{\partial X_{tj}}{\partial Y_{tj}} \\ &= \frac{1}{\varphi(Z_{tj})} \cdot \frac{1}{(X_{tj}/R_{tj}^{\phi_j} + 1)^2 R_{tj}^{\phi_j}} \cdot \frac{f_Y(Y_{tj})}{f_X(X_{tj})}, \end{aligned}$$

in which φ and Φ are, respectively, the density and the distribution function of a univariate standard Gaussian, $X_{tj} = F_X^{-1} \circ F_Y(Y_{tj})$, $Z_{tj} = g^{-1}(X_{tj}/R_{tj}^{\phi_j}) = \Phi^{-1}(1 - 1/(X_{tj}/R_{tj}^{\phi_j} + 1))$, f_Y is the marginal density of the observed data distribution, and f_X is the univariate density of the dependence model derived in (34). Then, as we have assumed temporal independence by introducing marginal temporal parameter, likelihoods across the independent time replicates are multiplied together for the joint likelihood.

C Computation

To estimate the posterior distribution of the model parameters, we sequentially update each parameter using an adaptive random walk Metropolis (RWM) algorithm (Shaby and Wells, 2010). Since we assume independence across time, we can update R_t 's in parallel across $t = 1, \dots, T$ at each MCMC iteration.

The probability integral transform in (13) and the Jacobian term in the likelihood (14) require evaluation of the marginal distribution and density functions of the dependence model $X(\mathbf{s})$. For general Stable variables S_1, \dots, S_K , this is difficult. However, under the special case of $\alpha = 1/2$, sometimes called a Lèvy distribution, we can obtain simpler analytical forms. Furthermore, fixing

$\alpha = 1/2$ sacrifices no flexibility with respect to the tail dependence characteristics described in Theorem 2.3. When $\alpha = 1/2$, the survival function for the mixture in (5) with the Type II (i.e. location-shifted) Pareto link function in 8 is

$$1 - F_{X_j}(x) = P(R_j^{\phi_j} W_j > x) = \sqrt{\frac{\bar{\gamma}_j}{2\pi}} \int_0^\infty \frac{r^{\phi_j-3/2}}{x + r^{\phi_j}} \exp\left\{-\frac{\bar{\gamma}_j}{2r}\right\} dr. \quad (33)$$

Using the Type II Pareto link function, rather than the standard Pareto, does not change the tail properties but can be advantageous for MCMC sampling because it aligns the support of the random scaling factor and the transformed Gaussian process. The trade-off is that the Type II Pareto, unlike the standard Pareto, does not give a closed form for the univariate distribution function for $X_j(s)$, and therefore requires numerical integration. Using Leibniz rule to take derivative with respect to x , we can get the univariate density function for $X_j(s)$,

$$f_{X_j}(x) = \sqrt{\frac{\bar{\gamma}_j}{2\pi}} \int_0^\infty \frac{r^{\phi_j-3/2}}{(x + r^{\phi_j})^2} \exp\left\{-\frac{\bar{\gamma}_j}{2r}\right\} dr, \quad (34)$$

which also requires numerical integration.

We evaluate the numerical integrals (e.g. the univariate distributions (33) and density functions (34) of the dependence model) using GSL libraries (Gough, 2009) in C++. The MCMC sampler is implemented in python, and the parallel updates are implemented via the mpi4py (Dalcin and Fang, 2021) module/interface to OpenMPI. After parallelization, on an AMD Milan EPYC CPU, running a chain, on datasets of 500 spatial locations and 64 time replicates, to approximately 15,000 iterations takes about 270 hours. The vast majority of this time is spent performing the numerical integration required by the joint fitting of the marginal and dependence models.

Implementation of the model and the data underlying this article are available in the GitHub repository, at https://github.com/muyangshi/GEV_ScaleMixture/tree/main/code.

D Additional Results on Simulation Study

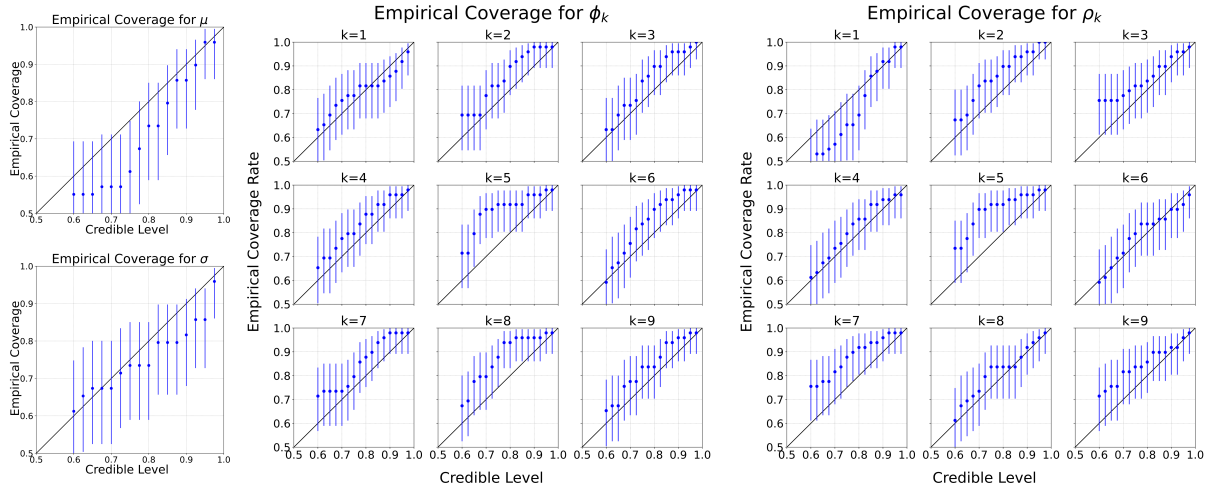


Figure 11: Empirical coverage rates of credible intervals of the marginal parameters μ and σ (left), the dependence parameters ϕ_k , $k = 1, \dots, 9$ (middle), and ρ_k , $k = 1, \dots, 9$ (right), in simulation scenario 2.

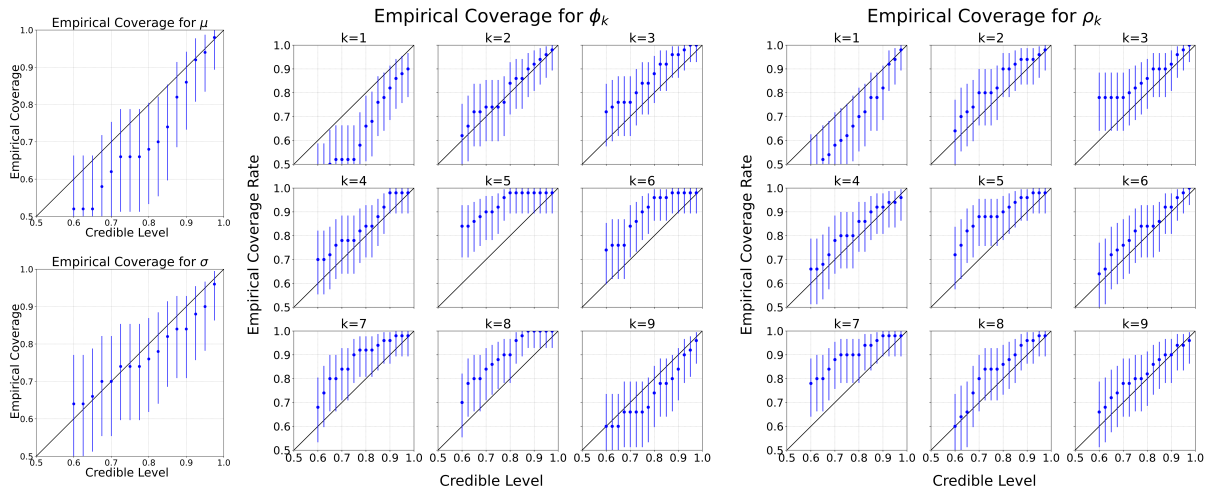


Figure 12: Empirical coverage rates of credible intervals of the marginal parameters μ and σ (left), the dependence parameters ϕ_k , $k = 1, \dots, 9$ (middle), and ρ_k , $k = 1, \dots, 9$ (right), in simulation scenario 3.

E Additional Results on Data Analysis

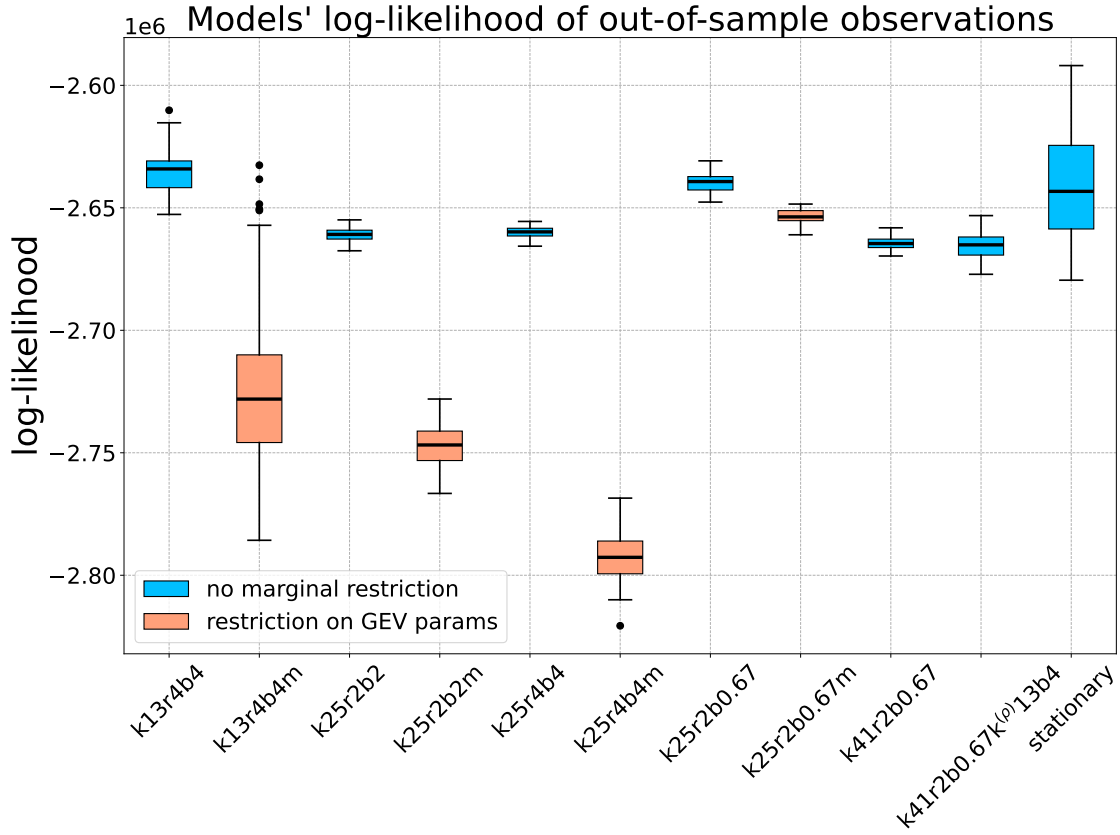


Figure 13: Boxplots of predictive log-likelihood for the eleven models. Higher log-likelihood is better. “Blue” models estimate the GEV parameters in the MCMC process, while the “orange models” have some restrictions on their marginal model parameters; “orange models” perform worse than their “blue counterparts”.

Table 1: Eleven model configurations spanning different knot grids, spatial extent of basis functions, and constraints on the marginal parameters. Model naming convention is as follows: k , r , b , and m respectively denote the number of knots, radius of the compact Wendland kernel, the bandwidth of the Gaussian kernel, and restriction indicator on marginal GEV parameters. Here the effective range refers to the distance at which the Wendland kernel function becomes 0 (as it is compact) or when the Gaussian kernel function drops below 0.05. The tenth model has a different configuration for S, ϕ versus ρ ; the eleventh model is the stationary [Huser and Wadsworth \(2019\)](#) process.

Model Name	Specification			
1. k13r4b4	Component	S	ϕ	ρ
	# of knots	13	13	13
	Effective Range	4	4.89	4.89
	Constraint	None		
3. k25r2b2	Component	S	ϕ	ρ
	# of knots	25	25	25
	Effective Range	2	3.46	3.46
	Constraint	None		
5. k25r4b4	Component	S	ϕ	ρ
	# of knots	25	25	25
	Effective Range	4	4.89	4.89
	Constraint	None		
7. k25r2b0.67	Component	S	ϕ	ρ
	# of knots	25	25	25
	Effective Range	2	2	2
	Constraint	None		
9. k41r2b0.67	Component	S	ϕ	ρ
	# of knots	41	41	41
	Effective Range	2	2	2
	Constraint	None		
Model Name	Specification			
2. k13r4b4m	Component	S	ϕ	ρ
	# of knots	13	13	13
	Effective Range	4	4.89	4.89
	Constraint	fix μ, σ, ξ		
4. k25r2b2m	Component	S	ϕ	ρ
	# of knots	25	25	25
	Effective Range	2	3.46	3.46
	Constraint	fix μ, σ, ξ		
6. k25r4b4m	Component	S	ϕ	ρ
	# of knots	25	25	25
	Effective Range	4	4.89	4.89
	Constraint	fix μ, σ, ξ		
8. k25r2b0.67m	Component	S	ϕ	ρ
	# of knots	25	25	25
	Effective Range	2	2	2
	Constraint	fix ξ		
10. k41r2b0.67k ^(ρ) 13b4	Component	S	ϕ	ρ
	# of knots	41	41	13
	Effective Range	2	2	4.89
	Constraint	None		
11. stationary	Component	S	ϕ	ρ
	# of knots	1	1	1
	Effective Range	∞	∞	∞
	Constraint	None		

Table 2: Posterior mean and 95% equi-tail credible interval of the $k13r4b4$ model.

Knot	ϕ - Posterior mean 95% credible interval	ρ - Posterior mean 95% credible interval
1	0.291 (0.058, 0.661)	1.605 (0.060, 4.488)
2	0.229 (0.045, 0.522)	1.636 (0.061, 4.186)
3	0.343 (0.061, 0.786)	1.407 (0.061, 3.700)
4	0.234 (0.036, 0.575)	1.314 (0.045, 4.063)
5	0.171 (0.033, 0.448)	2.061 (0.122, 4.145)
6	0.171 (0.039, 0.526)	2.464 (0.102, 6.026)
7	0.393 (0.118, 0.769)	1.461 (0.054, 3.662)
Knot	ϕ - Posterior mean 95% credible interval	ρ - Posterior mean 95% credible interval
8	0.15 (0.034, 0.416)	2.257 (0.153, 4.915)
9	0.358 (0.110, 0.632)	0.053 (0.002, 0.133)
10	0.303 (0.081, 0.640)	0.049 (0.002, 0.147)
11	0.209 (0.045, 0.498)	0.581 (0.489, 0.649)
12	0.15 (0.043, 0.319)	0.211 (0.053, 0.504)
13	0.163 (0.039, 0.338)	0.843 (0.690, 0.930)